NUMERICAL ANALYSIS OF FLOW AND HEAT TRANSFER CHARACTERISTICS OF GYROID TYPE STRUCTURES WITH TRIPLY PERIODIC MINIMAL SURFACES

A Thesis

by

Kourosh Naji

Submitted to the
Graduate School of Sciences and Engineering
in Partial Fulfillment of the Requirements for
the Degree of

Master of Science

in the
Department of Mechanical Engineering

Özyeğin University
September 2024

NUMERICAL ANALYSIS OF FLOW AND HEAT TRANSFER CHARACTERISTICS OF GYROID TYPE STRUCTURES WITH TRIPLY PERIODIC MINIMAL SURFACES

Advisor: Assoc. Prof. Özgür Ertunç, Özyeğin University
Coadvisor: Assist. Prof. Altuğ Melik Başol, University of Özyeğin

Approved by:

Assoc. Prof. Özgür Ertunç, Advisor
Dept. of Mechanical Eng.
Özyeğin University

Prof. M. Pınar Mengüç
Dept. of Mechanical Eng.
University of Özyeğin

Assoc. Prof. Tamer Çalışır
Dept. of Mechanical Eng.
Gazi University

Date Approved: August 9, 2024

To my beloved father and mother I extend my heartfelt gratitude to both of you. Your unwavering support and presence have been the cornerstones of my entire life. Your constant encouragement and guidance have shaped my academic pursuits and the person I have become. From my earliest education stages, you instilled a deep appreciation for knowledge and a relentless pursuit of excellence. Your dedication has reminded me that I am never alone on this journey. My dear friends, Thank you for your unwavering support and encouragement throughout this journey. Your friendship has been a source of strength and joy, motivating me to strive for excellence. I am truly grateful for the laughter, late-night study sessions, and constant reminders that I am never alone.

ABSTRACT

The popularity of additive manufacturing has increased interest in using triply periodic minimal surfaces (TPMS) in engineering applications due to their potential for superior mechanical, heat, and mass transfer properties. This study aims to understand the relationship between the properties defining gyroid TPMS structures, energy losses, heat transfer, and flow structure. For this purpose, the pressure drop-flow rate characteristics of two printed TPMS structures are measured in the first stage. The TPMS structures have the same porosity but differ in the frequency of gyroids. Later, flow simulations are conducted by using two methods: implicit unsteady incompressible Large Eddy Simulations (LES) equations along with the subgrid-scale model and steady incompressible Reynolds Averaged Navier -Stokes (RANS) equations along with the k-epsilon turbulence model. Although the simulated pressure drops do not perfectly match the measured ones, the experiments and simulations show that TPMS with high frequency creates less pressure drop over the whole range of mass flow rates. The simulation results revealed the same heat transfer rate characteristic for both frequencies. The difference in the pressure drop is investigated by looking at how much energy dissipation occurs near and away from the wall.

ÖZETÇE

Katmanlı üretimin popülaritesinin artması, üstün mekanik, ısı ve kütle transferi özelliklerine sahip olma potansiyelleri nedeniyle mühendislik uygulamalarında üçlü periyodik minimal yüzeylerin (TPMS) kullanımına olan ilgiyi artırmıştır. Bu çalışma, gyroid TPMS yapılarını tanımlayan özellikler, enerji kayıpları, ısı transferi ve akış yapısı arasındaki ilişkiyi anlamayı amaçlamaktadır. Bu amaçla, ilk aşamada iki basılmış TPMS yapısının basınç düşüşü-akış hızı özellikleri ölçülmüştür. Bu çalışmada TPMS yapıları aynı gözenekliliğe sahip ve gyroidlerin frekansı açısından farklılık vardır. Daha sonra, akış simülasyonları iki yöntem kullanılarak gerçekleştirilmiştir: implicit unsteady incompressible Large Eddy Simulations (LES) equations along with the subgrid-scale model and steady incompressible Reynolds Averaged Navier -Stokes (RANS) equations along with the k-epsilon turbulence model. Simüle edilen basınç düşüşleri, ölçülenlerle mükemmel bir şekilde eşleşmese de, deneyler ve simülasyonlar, yüksek frekanslı TPMS'in tüm kütle akış hızı aralığında daha az basınç düşüşü yarattığını göstermektedir. Simülasyon sonuçları, her iki frekans için de aynı ısı transferi oranı özelliğini ortaya koymuştur. Basınç düşüşündeki fark, enerji dağılımının duvara yakın ve uzak bölgelerde ne kadar gerçekleştiğine bakılarak incelenmiştir.

ACKNOWLEDGEMENTS

I express my deepest gratitude to my advisor and co-advisor, Assoc. Prof. Özgür Ertunç and Assist. Prof. Altuğ Melik Başol, for their invaluable guidance, support, and encouragement throughout this research.

I would also like to extend my heartfelt thanks to my friends and colleagues, Hanieh Farahnak Shandi, Sirri Ahmet Kasidecioğlu, Mohammad Bagheri, Onur Şen, Aziz Mert Karul, Alper Akardere, and Oğuzhan Aşik for their unwavering support. Their constructive feedback, moral support, and constant encouragement have been a source of great motivation.

Lastly, I thank my family for their unconditional love and support. Their faith in me has been my driving force throughout this journey.

TABLE OF CONTENTS

LIST OF TABLES

LIST OF FIGURES

LIST OF NOMENCLATURE

A	Wet surface area, p. 14.
a_f	Face area vector, p. 16.
C_p	Specific heat capacity, p. 15.
C_w	Model coefficient, p. 18.
Δ	Grid filter width, p. 18.
ΔP	Pressure drop, p. 31.
D_h	Hydraulic diameter, p. 14.
$\dot{m}$	Mass flow rate, p. 30.
f_b	Body forces, p. 17.
I	Identity tensor, p. 17.
k	Thermal conductivity, p. 16.
k	von Karman constant, p. 18.
k_t	Turbulent thermal conductivity, p. 15.
μ	Dynamic viscosity, p. 14.
μ_t	Subgrid-scale turbulent viscosity, p. 18.
ν	Laminar viscosity, p. 20.
$\nu_{t,eff}$	Effective viscosity, p. 20.
$\overline{p}$	Mean pressure, p. 15.
$\overline{T}$	Mean temperature, p. 15.
$\overline{U}_i$	Mean velocity, p. 15.
$\overline{u_i'u_j'}$	Reynolds stress tensor, p. 15.
P	Wet surface perimeter, p. 14.
ϕ	Iso-surfaces offset value, p. 9.
q	Heat transfer rate, p. 15.
q_f''	Face heat flux vector, p. 16.

Re	Reynold number, p. 14.
ρ	Density, p. 14.
s	The length of the unit cell, p. 9.
S	Mean strain rate tensor, p. 18.
S_d	Tensor, p. 19.
S_w	Deformation parameter, p. 18.
T	Stress tensor, p. 18.
$\tilde{E}$	Filtered total energy, p. 17.
$\tilde{p}$	Filtered pressure, p. 17.
$\tilde{\mathbf{q}}$	Filtered heat flux, p. 17.
$\tilde{\mathbf{T}}$	Filtered stress tensor, p. 17.
$\tilde{\mathbf{v}}$	Filtered velocity, p. 17.
T_{SGS}	Subgrid-scale stress, p. 18.
U	Velocity, p. 14.
V	Cell volume, p. 18.

CHAPTER I

INTRODUCTION

During the past three decades, cellular materials' structural and functional characteristics have been the subject of substantial research. Other researchers reported that they are frequently used in heat management [1, 2], tissue engineering [3, 4], impact absorption systems [5], vibration-damping mechanisms [6], membranes [7, 8], and other areas [9, 10, 11]. The general overview and application of TPMS structures are illustrated in Figure 1.

Triply periodic minimal surfaces (TPMS) are a particularly captivating class of mathematical surfaces defined by repeating patterns with minimal surface area. Among these structures, the Gyroid, with its intricate and self-intersecting network, stands out for its unique geometric properties.

Huang et al. [12] has shown that the composition of the material, a change in the cell of the porous structure, directly affects global performance parameters, such as the heat transfer coefficient and pressure drop. Femmer et al. [7] has shown that the Gyroid can be investigated as a heat exchanger because of its high surface-to-volume ratios. Also, Baobaid et al. [1] demonstrated the superior thermal performance of TPMS heat sinks compared to traditional pin-fin heat sinks, highlighting the potential of these geometries for advanced cooling solutions enabled by additive manufacturing.

The study by Iyer et al. [13] provides a comprehensive numerical analysis of the friction factors and Nusselt numbers of TPMS and PNS structures, demonstrating their superior performance as heat exchangers compared to conventional tubular designs. According to Moradmand & Sohankar [14], The Gyroid structure has been demonstrated to significantly outperform traditional tube banks as heat exchangers, with up to 24% higher performance evaluation coefficient (PEC) and a 40% increase in the Nusselt number, making it a promising candidate for advanced thermal management systems in both low and high Reynolds number regimes.

The study by Ansari & Duwig [15] reveals that gyroid TPMS heat sinks outperform conventional pinfin heat sinks in thermal management due to their intricate 3D helical flow structure, which enhances heat transfer efficiency. Despite this advantage, the gyroid design is associated with higher pressure drops and increased pumping power, indicating a need for further optimization to balance thermal performance with operational costs. The study by Lee et al. [16] introduces a novel design methodology using mathematical filtering to locally modify the morphology of a TPMS channel, resulting in enhanced fluid flow performance. By applying sigmoid functions to adjust the signed distance field (SDF) distribution, the study demonstrates a 20% reduction in pressure drop with only a 2.6% volume change. The methodology effectively decreases flow resistance in the inlet and outlet regions, offering an efficient approach for optimizing TPMS structures in complex geometries. This local filtering technique could be extended to various engineering applications, including thermo-fluidic components and lightweight structures, with the potential for further development in three-dimensional filtering schemes.

Alteneiji et al. [17] evaluates the performance of compact crossflow heat exchangers based on gyroid and primitive TPMS structures using 3D CFD modeling with STAR-CCM+. The research explores the heat transfer effectiveness and pressure drop characteristics across a range of NTU values and heat capacity ratios. The findings indicate that the gyroid TPMS structure significantly enhances heat exchanger effectiveness, showing up to a 35% improvement in effectiveness compared to traditional designs. In contrast, the primitive TPMS structure exhibits inconsistent performance improvements. The study highlights the potential of TPMS-based heat exchangers to achieve high convection heat transfer coefficients and low-pressure drops, with further research planned to investigate additional TPMS structures and fluids.

The study by Khalil et al. [18] investigates forced convection heat transfer in TPMS-based heat sinks with lattice topologies, specifically focusing on Diamond and Gyroid structures in solid and sheet networks. Through numerical simulations and experimental validation, the research finds that the G-Solid heat sink exhibits the lowest friction factor due to its minimal surface area and largest pore size. In terms of thermal performance, the G-Sheet configuration demonstrates the highest area heat transfer coefficient and lowest thermal resistance owing to its extensive surface area. The D-Solid heat sink also achieves the highest thermal efficiency for a given pumping power. The findings highlight the potential of TPMS-based heat sinks for advanced thermal management systems, showcasing their advantages in pressure drop and heat transfer performance.

In another study by Ali et al. [19], the free convection heat transfer performance of architected heat sinks based on triply periodic minimal surfaces (TPMS) was thoroughly investigated using 3D CFD modeling with the Star-CCM+ platform. The research focused on three TPMS-based heat sinks—Diamond-solid, Gyroid-solid, and Gyroid-sheet networks. The study evaluated key performance metrics such as heat transfer coefficients and surface temperatures, comparing them across different heat sink designs. Findings indicated that while the solid-network heat sinks had similar surface areas, the Gyroid-sheet network featured nearly double the surface area of the solid networks. The results demonstrated that convective heat transfer was dominant up to a heat rate of 25 W, beyond which molecular diffusive flux became more significant. Among the designs, the Diamond network exhibited the highest convection heat transfer coefficient, highlighting its superior capability in heat dissipation compared to the other TPMS-based configurations.

In a recent study by Zimmer et al. [20], the impact of different 3D printing techniques on the properties of structured packings with triply periodic minimal surfaces

(TPMS) was explored through simulations and experiments. The research compared stereolithography (SLA), selective laser sintering (SLS), and multi-jet fusion (MJF) methods, finding that SLA produced packings with the lowest porosity and rugosity, while MJF showed the highest. The study demonstrated that the choice of printing technique significantly influences packing properties, underscoring the need for careful selection of manufacturing methods to optimize performance.

Expanding on earlier work, Barakat et al. [21] conducted an in-depth analysis of TPMS configurations, focusing on Fischer Koch S, Gyroid, Diamond, and SplitP lattices. The study found that the Fischer Koch S lattice outperformed the others in convective heat transfer rates and Nusselt numbers through numerical simulations and experimental validation due to optimized flow patterns and increased surface contact area. However, it also encountered significant pressure drops at higher Reynolds numbers, highlighting the need for further optimization to enhance its potential in advanced thermal management applications.

In another study, Liu et al. [22] explore TPMS-based heat exchangers (HXs) produced via additive manufacturing (AM). The study assesses heat transfer coefficients, pressure drops, and thermal capacities, focusing on the impact of wall thickness, lattice density, and materials. Results show that when thermal conductivity exceeds 100 W/m·K, gyroid HXs are less affected by changes in thickness and conductivity. The successful fabrication and testing of 20 kW aluminum HXs, with performance matching theoretical predictions, marks a significant advancement in TPMS HX development, highlighting their potential in advanced thermal management.

Despite the demonstrated effectiveness of Gyroid structures in these applications, current research has not fully explored how lateral modifications, specifically in the y and z directions, can influence their thermal and fluid dynamics characteristics. This presents an opportunity to investigate whether such modifications can optimize the performance of these structures, particularly in heat transfer and pressure drop applications.

1.1 Research Gap and Motivation

While previous studies have established the Gyroid TPMS structure as a strong candidate for various applications, particularly in heat management, the effects of altering the geometry properties of these structures in the lateral (y and z) directions to optimize their performance remain largely unexplored. Table1 summarizes key studies on triply periodic minimal surfaces (TPMS) structures, detailing the focus of each study and the variations analyzed, including material composition, geometric configurations, and manufacturing techniques. This research seeks to fill the existing gap by investigating how these lateral modifications in geometrical properties of TPMS structures impact the heat transfer rates and pressure drop characteristics of Gyroid structures. Understanding these effects could lead to significant advancements in designing and optimizing high-performance heat exchangers and other related devices.

1.2 Hypothesis

Hypothesis: *Exploring the effects of modifying the geometrical properties of Gyroid TPMS structure in alternative configurations may reveal changes in heat transfer rates and pressure drop characteristics. These modifications could potentially optimize performance, but the specific outcomes require detailed investigation.*

1.3 Objectives

Primary Objective: To investigate the impact of lateral modifications in the Gyroid TPMS structures on their thermal and fluid dynamics characteristics.

Secondary Objectives:

- To compare the heat transfer rates and pressure drops between modified and unmodified Gyroid structures.

- To validate the CFD simulation results with experimental data obtained from 3D-printed TPMS structures.

- To explore the practical implications of these modifications for the design of high-performance heat exchangers.

1.4 Methodology

This research uses a combined computational and experimental approach to analyze the heat transfer and fluid flow characteristics of modified Gyroid TPMS structures.

Computational Approach: Computational Fluid Dynamics (CFD) analyses were conducted using RANS and LES models to simulate the thermal and fluid dynamics in the modified and unmodified Gyroid structures. These simulations aimed to predict the heat transfer rates and pressure drops for different modifications of the Gyroid structure in the y and z directions.

Experimental Validation: To validate the simulation results, two distinct gyroid geometries, each modified in the y and z directions were fabricated using 3D printing. The pressure drop-flow rate characteristics of these printed TPMS structures were experimentally measured and compared to the numerical predictions. During the fabrication process, dimensional limits were encountered due to the constraints inherent in the 3D printing technology, which influenced the printed structures' final geometry and surface roughness. These limitations were carefully considered when interpreting the results, as they could impact the accuracy of the pressure drop measurements. Additionally, the measurement methods employed were selected to account for potential deviations caused by these dimensional constraints, ensuring that the experimental data provides a reliable comparison to the numerical models.

Analysis: The data from the simulations and experiments were thoroughly analyzed to conclude the impact of the structural modifications. The study examined how these modifications influenced the overall performance of the Gyroid structures

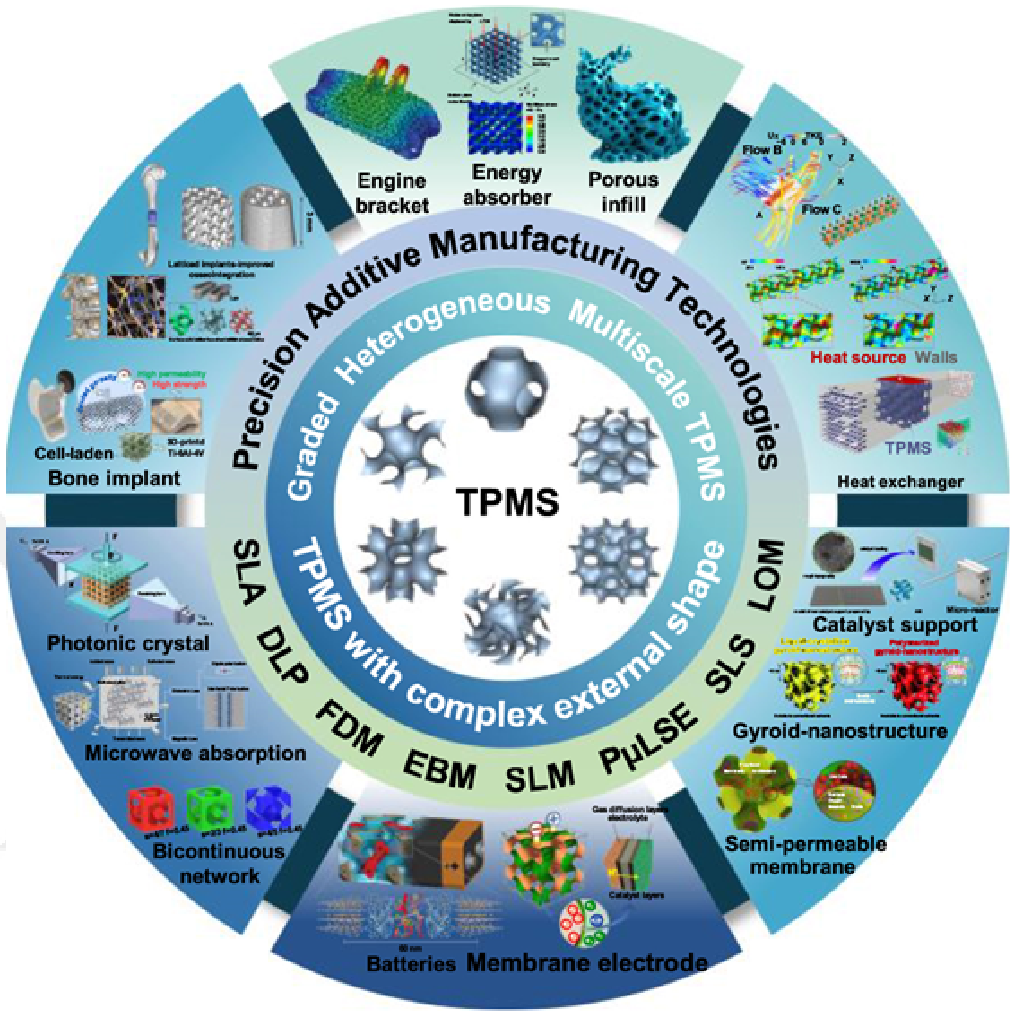

Figure 1: Overview of the TPMS structures [23].

in terms of heat transfer efficiency and pressure drop reduction.

1.5 Conclusion

This study explores the gyroid TPMS for improved heat transfer and pressure drop characteristics. Computational and experimental investigations, in a complementary way, offer an understanding of thermal and flow dynamics with greater confidence in the inquiry's findings. By addressing the gap in current research, this work aims to advance the application of Gyroid TPMS structures in heat management and other related fields.

Table 1: Summary of Studies on TPMS Structures and Their Variations.

Study	Focus	Variations Analyzed
[12]	Influence of material composition	Material composition and cell structure affecting heat transfer coefficient and pressure drop
[7]	TPMS as heat exchangers	Application of Gyroid TPMS for heat exchangers due to high surface-to-volume ratios
[1]	TPMS heat sinks	Superior thermal performance of TPMS heat sinks compared to traditional pin-fin heat sinks
[13]	Numerical analysis of TPMS	Friction factors and Nusselt numbers for TPMS and PNS structures showing superior heat exchanger performance
[14]	Gyroid performance	Gyroid structure outperforming traditional tube banks with higher PEC and Nusselt number
[15]	TPMS heat sinks in thermal management	Enhanced heat transfer efficiency of gyroid TPMS heat sinks with challenges in pressure drops
[16]	Local modification of TPMS morphology	Mathematical filtering to locally modify TPMS channel morphology for optimized fluid flow performance
[17]	Crossflow heat exchangers	Heat transfer effectiveness and pressure drop characteristics of gyroid and primitive TPMS structures
[18]	Forced convection in TPMS heat sinks	Friction factor, heat transfer coefficient, and thermal resistance in Diamond and Gyroid TPMS structures
[19]	Free convection in TPMS heat sinks	Free convection heat transfer in Diamond-solid, Gyroid-solid, and Gyroid-sheet TPMS-based heat sinks
[20]	3D printing techniques for TPMS packings	Impact of different 3D printing techniques (SLA, SLS, MJF) on TPMS-based structured packings
[21]	Fischer Koch S lattice performance	Performance of Fischer Koch S, Gyroid, Diamond, and SplitP lattices in convective heat transfer and pressure drops
[22]	TPMS heat exchangers produced via AM	Heat transfer coefficients, pressure drops, and thermal capacities of gyroid HXs with variations in wall thickness, lattice density, and material

CHAPTER II

METHODOLOGY

In this chapter, some of the concepts that will be used throughout the work will be introduced, along with the objective of this work.

2.1 TPMS construction

The following equation can mathematically define Gyroid TPMS according to [24]:

$$\text{Gyroid:}\quad \sin\left(\frac{2\pi x}{s}\right)\cdot\cos\left(\frac{2\pi y}{s}\right)+\sin\left(\frac{2\pi y}{s}\right)\cdot\cos\left(\frac{2\pi z}{s}\right)+\sin\left(\frac{2\pi z}{s}\right)\cdot\cos\left(\frac{2\pi x}{s}\right)=\phi \tag{1}$$

Where s is the length of the unit cell, and ϕ is used to create iso-surfaces with an offset value. Using the above equation as a guide, the surfaces were made with the nTop 4.16.3.0 version software. The s values for the y and z components were adjusted correspondingly to alter the frequency of the surfaces in the lateral directions. Figures 2a and b illustrate the selection of s for the high- and low-frequency geometries, which are 3π mm and 5π mm, respectively. The s values for the x components remain unchanged. As a result, the same number of rows were generated along the flow direction. The space between each row in both topologies is 12.5 mm, as seen in Figures 2c and d.

The aim is to observe the effect of frequency at constant porosity on the pressure drop and heat transfer. Therefore, the offset value *phi* varied in both geometries to keep the porosity value equal to 0.5. In conclusion, the thickness of the wall varied to keep the porosity constant. The porosities of both high- and low-frequency TPMS structures were experimentally determined. The printed geometry was filled with water, and a transparent plastic measuring cup measured the water's volume through

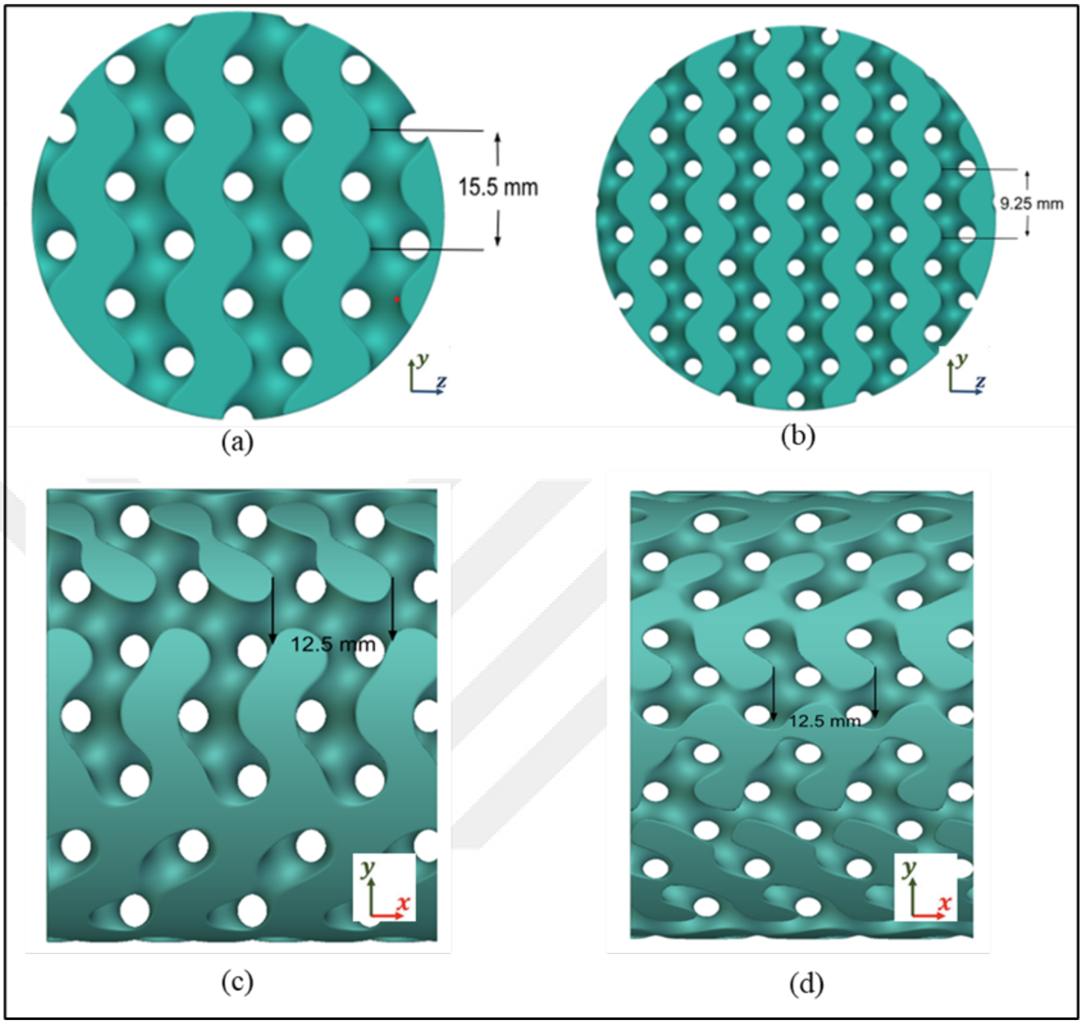

Figure 2: Topology and dimensions of TPMS structures (a,c) low frequency and (b,d) high frequency.

the porous media. Measured water volume (void volume) divided by the total volume of the porous medium surrounded by the cylinder using the porosity equation, it was observed that the porosity remained constant for both geometries.

Five separate experiments were conducted to evaluate the porosity of 3D-printed geometries, as summarized in Table 2. It is important to note that uncertainties may arise in the porosity calculation experiments. These uncertainties can be attributed to several factors, including the quality of the 3D-printed geometries and the presence of cavities within these structures. Such cavities may allow for unintended fluid flow within the printed geometries, affecting the accuracy of the measurements. Additionally, some calculations were performed manually, introducing potential sources of error. Consequently, these factors collectively contribute to the observed variability in the porosity measurements. These calculations ensure that our porosity remained approximately 50 percent in both geometries. Furthermore, they verify that our printed geometries have similar porosity to those used in the simulations. This consistency between experimental and simulated porosity values enhances our computational models' reliability and supports our experimental methods' validity.

Table 2: Experimental porosity calculations.

Experiment	**Low-frequency TPMS**	**High-frequency TPMS**
1	49.8	50.9
2	50.8	50
3	51.3	49.5
4	49.6	50.2
5	50.6	49.3
Average porosity	50.42	49.98

The dimensions selected for the TPMS structures in this study were carefully chosen based on the construction capabilities and limitations of the 3D printers available at the OpenFab lab at Özyeğin University. While theoretically, a wide range of geometric variations could be explored, practical constraints such as the resolution of the 3D printer, the minimum wall thickness achievable, and the overall structural integrity of the printed objects played a significant role in defining the feasible dimensions.

One key consideration was the ability of the printer to accurately reproduce the intricate features of the Gyroid TPMS, especially in the directions of the y and z where geometric modifications were applied. To balance structural fidelity and printability, the frequency parameters were set within a range that the printer could reliably produce without compromising the quality of the final structures. Additionally, maintaining a consistent row spacing of 12.5 mm along the flow direction was influenced by the need to ensure uniformity in the printed samples, which is critical for obtaining reliable experimental data.

These construction limitations also influenced the choice of offset values to achieve a porosity of approximately 50 percent. Maintaining consistent porosity across different geometries was essential for validating the computational models. The slight variations in porosity observed during the experimental measurements can be attributed to the inherent variability in the 3D printing process, which is affected by factors such as layer adhesion, material deposition, and small cavities within the printed structures.

In conclusion, the dimensions selected for this study represent a practical compromise between the ideal geometric configurations desired for optimal performance and the physical constraints imposed by the available 3D printing technology. This approach ensured that the printed TPMS structures were suitable for experimental validation and aligned closely with the simulated models, thereby enhancing the overall reliability of the research findings.

CHAPTER III

NUMERICAL SETUP

The computational domain, mesh generation, grid independence analysis, governing equations, and heat transfer coefficient calculation methods are covered in this part.

3.1 Computational domain and mesh generation

In the computational model, the cold air flowed through the porous medium. The temperature of the porous medium was kept constant at 353K, and the working fluid was cooled. An inlet temperature of 298K and a pressure of 1 atm were selected, where the physical properties became temperature-independent, and the effects of variable physical properties were excluded. The boundary conditions of the simulations were illustrated in Table 3. Figure 3 shows the computational domain's isometric, side, and front views. The unit cell sizes are 12.5 × 9.4 mm × 9.4 mm and 12.5 mm × 15.7 mm × 15.7 mm for high- and low-frequency topologies, respectively. The cylindrical block was placed at a distance of 39 mm from the inlet. An extended length of 12 mm was provided downstream of the block to avoid the influence of back pressure effects and reverse flow on the convergence, as well as heat transfer and pressure drop calculations.

Table 3: Boundary conditions employed in the simulations.

Boundary condition	**Fluid flow**	**Thermal**
Inlet	$u = U_{in}$ $v = 0$ $w = 0$	$T = T_0 = 298K$
TPMS walls	$V = 0$	$T_s = 353K$
Channel walls	$V = 0$	$\frac{\partial T}{\partial n} = 0$
Outlet	$\frac{\partial (u,v,w)}{\partial x} = 0$	$\frac{\partial T}{\partial x} = 0$

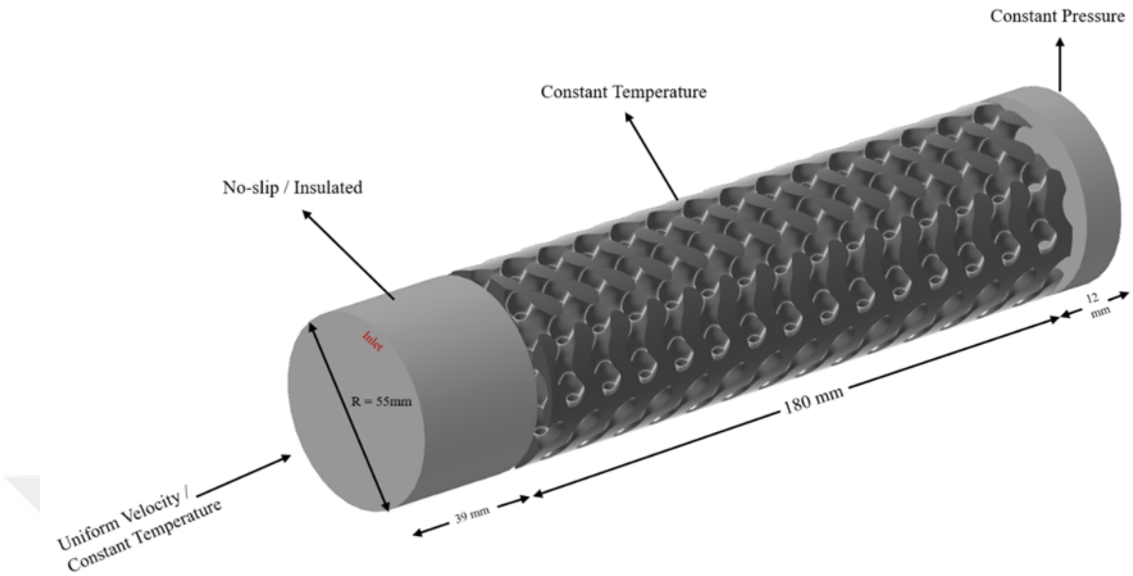

Figure 3: Isometric view of the computational domain with boundary conditions.

3.2 Governing equations and numerical models

Simulations and measurements have been performed over a Reynolds number range between 152 and 590, mostly in the turbulent regime. In TPMS structures, the hydraulic diameter (D_h) was employed instead of the conventional geometric length (d) due to the intricate and irregular nature of their geometry:

$$Re = \frac{\rho U D_h}{\mu} \tag{2}$$

Where,

$$D_h = \frac{4A}{P} \tag{3}$$

A is the wet surface area, P is the perimeter of the wet surface, ρ is density, U is velocity, and μ represents for dynamic viscosity. Given the intricate geometric nature of the gyroid structure, conventional methods for calculating the area and perimeter necessary to determine the hydraulic diameter are almost unfeasible. Consequently, a planar section was delineated at the inlet of the gyroid, and computation of the area and perimeter of the delineated plane was done using post-processing tools of the computational fluid dynamics (CFD) software.

3.2.1 Governing equations of RANS model

In this section, steady-state incompressible Reynolds-averaged Navier-Stokes (RANS) equations and the k-epsilon turbulence model were used for simulations. As a wall treatment model, the two-layer all y+ model is considered [25]. Air is the working fluid; its physical properties are shown in Table 4. The 3-D, steady-state, incompressible RANS equations are as follows:

Continuity:

$$\frac{\partial \overline{U}_i}{\partial x_i} = 0 \tag{4}$$

Momentum:

$$\rho \overline{U}_j \frac{\partial \overline{U}_i}{\partial x_j} = -\frac{\partial \overline{p}}{\partial x_i} + \frac{\partial}{\partial x_j}\left(\mu \frac{\partial \overline{U}_i}{\partial x_j} - \rho \overline{u_i' u_j'}\right) \tag{5}$$

Energy transport in the fluid domain:

$$\rho C_p \overline{U}_j \frac{\partial \overline{T}}{\partial x_j} = \frac{\partial}{\partial x_i}\left(k_t \frac{\partial \overline{T}}{\partial x_j}\right) \tag{6}$$

Where $\overline{U}_i$, $\overline{u_i' u_j'}$, $\overline{T}$,C_p, and $\overline{p}$ are the mean velocity, Reynolds stress tensor, mean temperature, specific heat capacity, and mean pressure values. The k-epsilon turbulence model is used, and turbulent thermal conductivity (k_t) is defined as:

$$k_t = \frac{\mu_t C_p}{Pr_t} \tag{7}$$

Numerical solutions were performed using a double precision StarCCM+ 20.3 finite volume solver. The governing equations of the model were discretized using a finite-volume method based on pressure. For pressure-velocity coupling, a segregated solver with a SIMPLE algorithm was used. A second-order scheme was employed to discretize the convective terms in the governing equations, and the pressure-velocity coupling was performed using the segregated temperature algorithm.

The heat transfer rate (q) was defined as,

$$q = \int q'' \cdot da = \sum_f q_f'' \cdot a_f \tag{8}$$

where,

$$q''_f = -k\nabla T \tag{9}$$

The heat transfer rate was calculated using the reporting feature within the STAR-CCM+ software. In these calculations, q''_f (W/m^2) is the face heat flux vector, k (W/mK) is the thermal conductivity, a_f is the face area vector, and q (W) is the heat transfer rate. When the heat flow direction aligns with the boundary normal direction, the heat transfer rate is reported as positive [26].

Table 4: Thermophysical properties of air.

Property	Unit	Value
Density, ρ	kg/m^3	1.204
Specific heat capacity, c_p	J/kgK	1007
Thermal conductivity, k	W/mK	0.02514
Dynamic viscosity, μ	kg/ms	0.00001825

3.2.2 Governing equations of LES model

In this part for simulations, unsteady incompressible Large Eddy Simulation (LES) equations along with the Wall-Adapting Local-Eddy Viscosity (WALE) sub-grid scale (SGS) model are used; hence, it is a more modern subgrid-scale model that uses a novel form of the velocity gradient tensor in its formulation [27, 28]. As a wall treatment model, all y+ is considered [25]. Air is the working fluid; its physical properties are shown in Table 4. The 3-D, unsteady-state, incompressible LES equations are as follows [26]:

$$\phi = \tilde{\phi} + \phi' \tag{10}$$

Where ϕ represents velocity components, pressure, energy, or species concentration, each solution variable ϕ is decomposed into a filtered value $\tilde{\phi}$ and a sub-filtered, or sub-grid, value ϕ'. Spatial filtering in LES eliminates the smaller eddies associated with higher frequencies, thus narrowing the range of scales that need to be resolved. This filtering can be implemented either explicitly or implicitly. Explicit filtering involves applying a filter function, like a box or Gaussian filter, to the discretized Navier-Stokes equations. The process of filtering a generic instantaneous flow variable is defined as follows:

$$\tilde{\phi}(t, \mathbf{x}) = \iiint_{-\infty}^{\infty} G(\mathbf{x} - \mathbf{x}', \Delta)\phi(t, \mathbf{x}')\, d\mathbf{x}' \tag{11}$$

Implicit filtering is used in Simcenter STAR-CCM+ software. In this method, the computational grid dictates the scales of eddies that are filtered out. Implicit filtering fully leverages the grid resolution and is typically less computationally demanding than explicit filtering. By substituting the decomposed solution variables into the Navier-Stokes equations, we derive equations for the filtered quantities. The filtered equations for mass, momentum, and energy transport are expressed as follows [23]:
Filtered mass:

$$\frac{\partial \rho}{\partial t} + \nabla \cdot (\rho \tilde{\mathbf{v}}) = 0 \tag{12}$$

Filtered momentum:

$$\frac{\partial}{\partial t}(\rho \tilde{\mathbf{v}}) + \nabla \cdot (\rho \tilde{\mathbf{v}} \otimes \tilde{\mathbf{v}}) = -\nabla \cdot \tilde{p}\mathbf{I} + \nabla \cdot \left(\tilde{\mathbf{T}} + \mathbf{T}_{SGS}\right) + \mathbf{f}_b \tag{13}$$

Filtered energy transport:

$$\frac{\partial}{\partial t}(\rho \tilde{E}) + \nabla \cdot (\rho \tilde{E} \tilde{\mathbf{v}}) = -\nabla \cdot \tilde{p}\tilde{\mathbf{v}} + \nabla \cdot \left(\tilde{\mathbf{T}} + \mathbf{T}_{SGS}\right) \tilde{\mathbf{v}} - \nabla \cdot \tilde{\mathbf{q}} + \mathbf{f}_b \tilde{\mathbf{v}} \tag{14}$$

Where ρ is density, $\tilde{\mathbf{v}}$ is the filtered velocity, $\tilde{p}$ is the filtered pressure, I is the identity tensor, $\tilde{\mathbf{T}}$ is the filtered stress tensor, f_b is the resultant of the body forces such as gravity or centrifugal forces, $\tilde{E}$ is the filtered total energy per unit mass, $\tilde{\mathbf{q}}$ is the filtered heat flux. The filtered equations are reformulated to resemble the unsteady RANS equations. However, the turbulent stress tensor corresponds to the subgrid-scale stresses in this case. These stresses arise from the interaction between the more significant, resolved eddies and the smaller, unresolved eddies. The subgrid-scale stresses (T_{SGS}) are modeled using the Boussinesq approximation, as shown below:

$$T_{SGS} = \frac{2\mu_t S^2}{3}(\mu_t \nabla \cdot \tilde{\mathbf{v}})\mathbf{I} \tag{15}$$

Where S is the mean strain rate tensor given by:

$$S = \frac{1}{2}(\nabla \bar{v} + \nabla \bar{v}^T) \tag{16}$$

In the above equation, $\bar{v}$ is the mean velocity and T states for the stress tensor. The subgrid-scale turbulent viscosity μ_t in equation number (15) must be described by a subgrid-scale model that accounts for the effects of small eddies on the resolved flow. Currently, the WALE subgrid-scale model was considered in the simulations [27]. Like the Smagorinsky SGS model, the WALE model also faces the issues of the model coefficient C_w. However, validations performed using Simcenter STAR-CCM+ software indicate that the WALE model is less affected by the value of this coefficient compared to the Smagorinsky model. A vital advantage of the WALE model is that it inherently provides accurate scaling at walls without needing any near-wall damping. Which states that:

$$\mu_t = \rho \Delta^2 S_w \tag{17}$$

ρ is the density, Δ states the length scale or grid filter width, and S_w is the deformation parameter. The length scale Δ is defined in terms of the cell volume V as:

$$\Delta = \begin{cases} C_w V^{1/3} & \text{if length scale limit is not applied} \\ \min(kd, C_w V^{1/3}) & \text{if length scale limit is applied} \end{cases} \tag{18}$$

Where C_w is a model coefficient equal to 0.544 based on the validation of the Simcenter STAR-CCM+ software, k is the von Karman constant equal to 0.41. The deformation parameter S_w in equation (17) is as follows:

$$S_w = \frac{S_d : S_d^{3/2}}{S_d : S_d^{5/4} + S : S^{5/2}} \tag{19}$$

The tensor S_d is defined as:

$$S_d = \frac{1}{2}\left[\nabla v \cdot \nabla v + (\nabla v \cdot \nabla v)^T\right] - \frac{1}{3}\,\mathrm{tr}(\nabla v \cdot \nabla v)I \tag{20}$$

Which I is the identity tensor.

3.3 Mesh independency study

3.3.1 grid resolution in RANS simulations

Since Gyroid geometry was made up of a curved shape, the block faces were sufficiently refined to guarantee that the mesh components adhered strictly to the geometry. A

Table 5: Mesh independency.

Mesh size	**Low mesh**	**Medium mesh**	**High mesh**
Pressure drop (Pa)	120.78	118.61	118.53

comprehensive mesh independence study was conducted to ensure our computational simulations' accuracy and reliability. This involved comparing the simulation results obtained using three mesh cell sizes at 3.85 (g/s) mass flow rate to identify the optimal mesh configuration demonstrated in Table 5, correspondingly low mesh is 1 million, medium mesh is 4 million, and high mesh is 6 million cells. The objective was to determine a mesh size that would yield consistent results, ensuring that further refinement would not significantly impact the outcomes. The mesh independence study confirmed that the medium mesh configuration balanced computational efficiency and accuracy. The negligible differences between the medium and fine meshes indicate that the selected mesh size is sufficiently refined to produce reliable simulation results. Therefore, this research adopted the medium mesh configuration for RANS simulations.

3.3.2 Grid resolution in LES simulations

The grid quality plays a crucial role in the accuracy and reliability of LES simulations. To ensure high-quality simulation results, it is imperative to specify an appropriate time step corresponding to the grid quality. One of the key parameters in this context is the Courant-Friedrichs-Lewy (CFL) number, which is considered less than 1 to ensure numerical accuracy. Figure 4 presents convective courant numbers for both geometries at a 3.36 (g/s) mass flow rate. this figure demonstrates the compliance of our simulations with the CFL condition. In addition to the CFL number, the LES IQ number is another crucial metric for assessing the adequacy of grid resolution in LES simulations. The LES IQ number should be greater than 0.8 [29] to ensure the simulation adequately resolves the turbulent scales of interest. Figure 5 depicts the LES IQ dispersion for high- and low-frequency TPMS structures at a 3.36 (g/s) mass flow rate. The results illustrated in Figures 4 and 5 collectively indicate that our simulations possess an acceptable grid resolution across the highest mass flow rate considered in this study.

The convective Courant numbers and LES IQ values confirm the high fidelity of our simulations, ensuring that the critical flow features and turbulence eddies are accurately captured. LES IQ number formulation is given by [30]:

$$LES\_IQ = \frac{1}{\left(1 + 0.05\left(\frac{\nu_{t,\mathrm{eff}}}{\nu}\right)\right)^{0.53}} \tag{21}$$

Where ν is laminar viscosity, and $\nu_{t,eff}$ denotes the effective viscosity, the sum of turbulent and laminar viscosity. The quality of the grid resolution is depicted in Figure 6. Approximately 9 million cells were considered in both simulations, in which Figures 6a and b represent the high-frequency and low-frequency TPMS mesh scene quality, respectively.

Furthermore, a detailed analysis of the dimensionless wall distance, y+, was performed for the simulations, particularly at a mass flow rate of 3.36. The y+ values

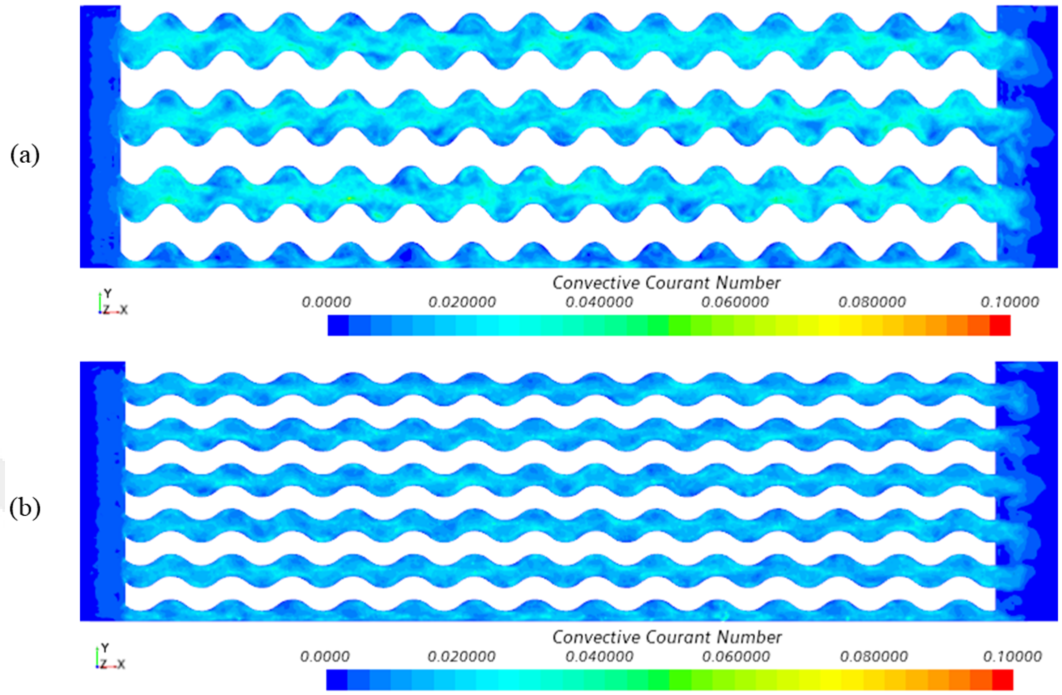

Figure 4: Courant number scene - (a)Low-frequency TPMS, (b)high frequency-TPMS.

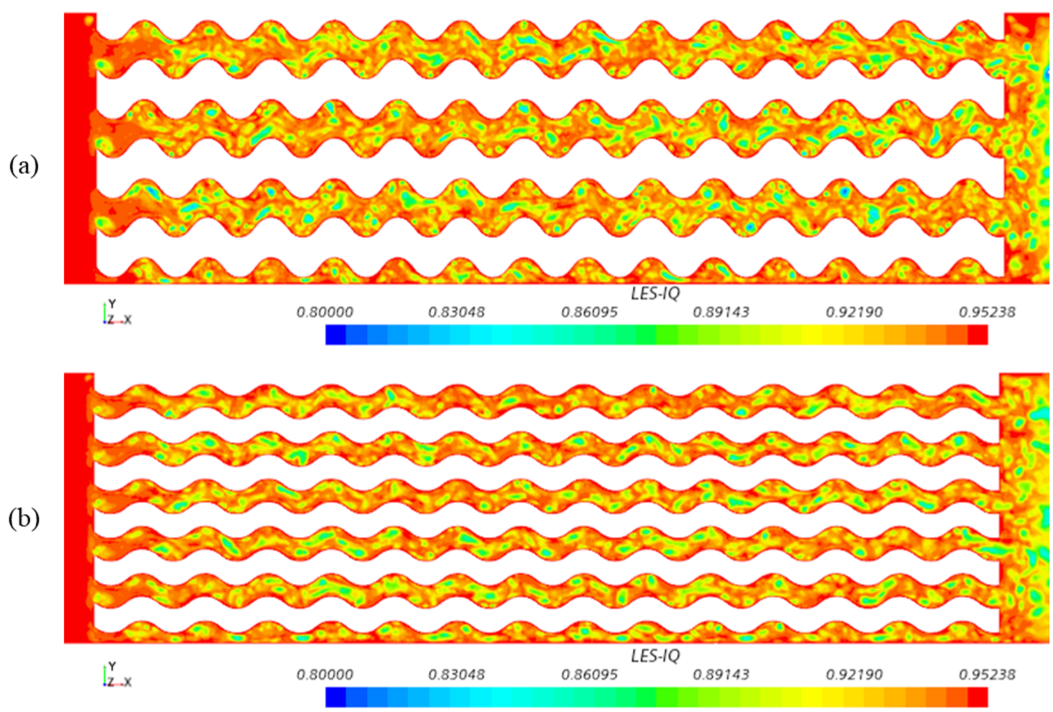

Figure 5: LESIQ scene - (a) Low-frequency TPMS, (b) High-frequency TPMS.

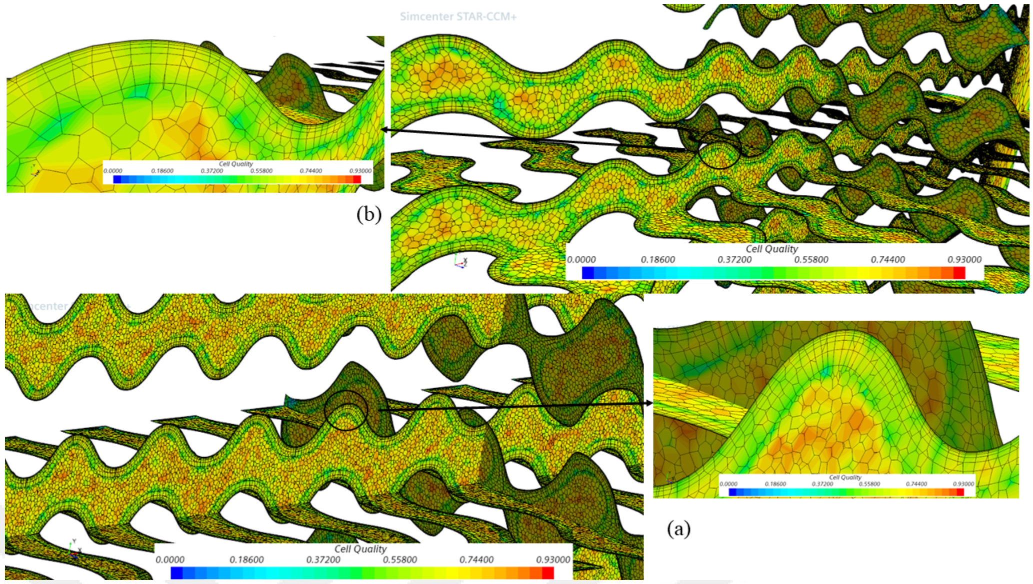

Figure 6: Mesh quality scene. (a) low-frequency TPMS, (b) high-frequency TPMS.

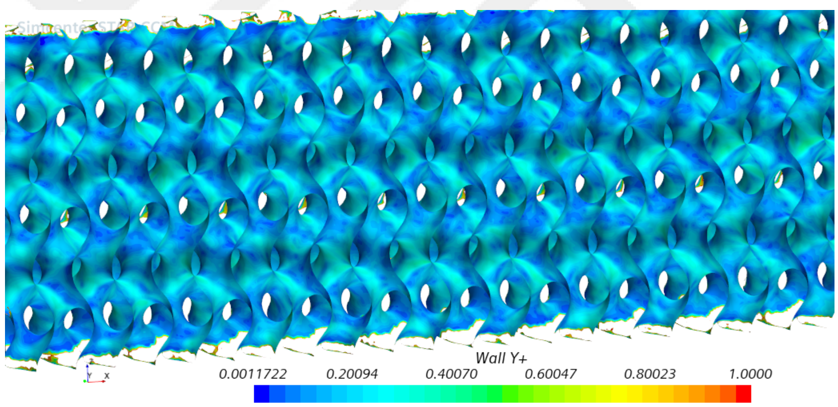

Figure 7: Y+ scene at 3.36(g/s) mass flow rate.

provide insight into the resolution of the boundary layer and are critical in ensuring that the near-wall turbulence is accurately captured. For LES, maintaining y+ values close to 1 is typically recommended, as this indicates that the first cell layer is within the viscous sublayer, where turbulence models can accurately resolve the flow. The analysis of y+ in this study, as depicted in Figure7, demonstrated that the mesh configuration was adequate for capturing the near-wall effects without requiring further refinement.

CHAPTER IV

EXPERIMENTAL SETUP

The fabrication of the TPMS structure utilized fused deposition modeling (FDM), a cost-effective and commonly employed technique compared to alternative printing methodologies. Employing PLA+ material and the Creality Endor Neo 3D printer machine, TPMS geometries were crafted.

Figures 8a and 9 illustrate the experimental setup, including essential components such as an air compressor with a capacity to operate within a mass flow rate range of 0.24g/s and 3.8g/s, interconnected pipes, a flow control valve, the VA525, compact inline flow meter from CS Instruments with a measurement range from 0.16 to 47.9 g/s and accuracy of ± 1,5 % measured value, ± 0,3 % full scale, along with ABB 2600T pressure transducer with accuracy of 0.05 per 1 (kPa) strategically placed at the inlet and outlet sections, ensure accurate measurement of pressure differentials.

Lastly, a honeycomb pattern, as shown in Figure 4b, provides a more uniform distribution of the fluid flow placed at the exit of the diffuser. The TPMS gyroid structure is encased within a cylindrical pipe with a radius of 2.75 cm and a length of 23 cm.

The consistent TPMS length of 18 cm is maintained in all geometries. High-pressure air originating from the air compressor is directed through a pipe. After passage through the flow control valve, the mass flow rate and air velocity were measured by a flowmeter.

A diffuser is introduced to facilitate the connection between the 2.54 cm piping and the test section with a diameter of 5.5 cm. A honeycomb pattern was located at the outlet part of the diffuser to ensure the flow passing through the diffuser

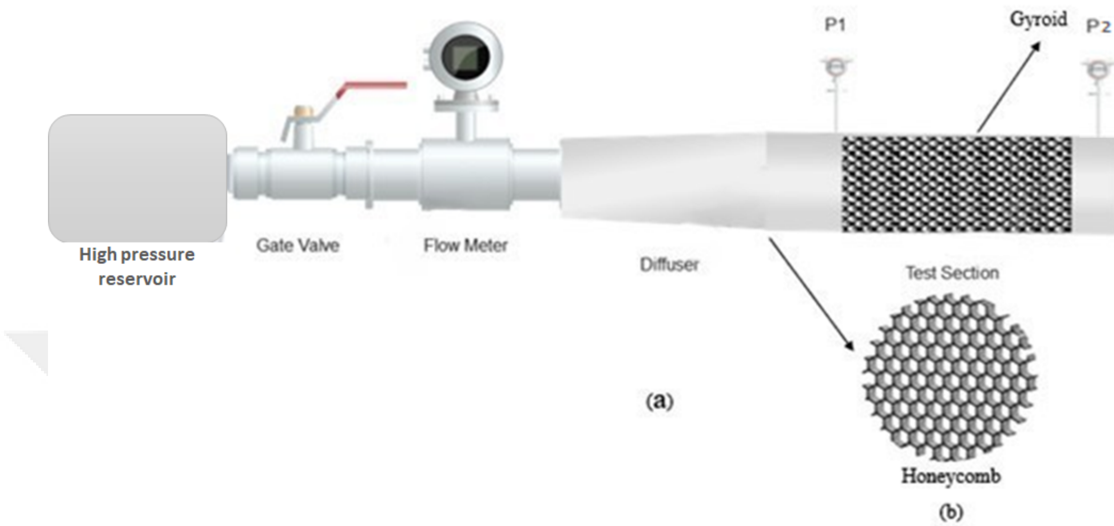

Figure 8: (a) The schematic experimental setup for evaluating the pressure drop, (b) honeycomb.

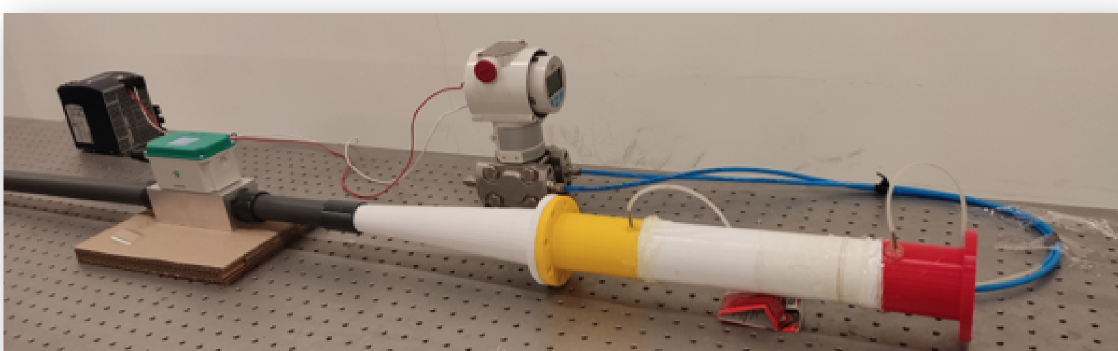

Figure 9: The experimental setup.

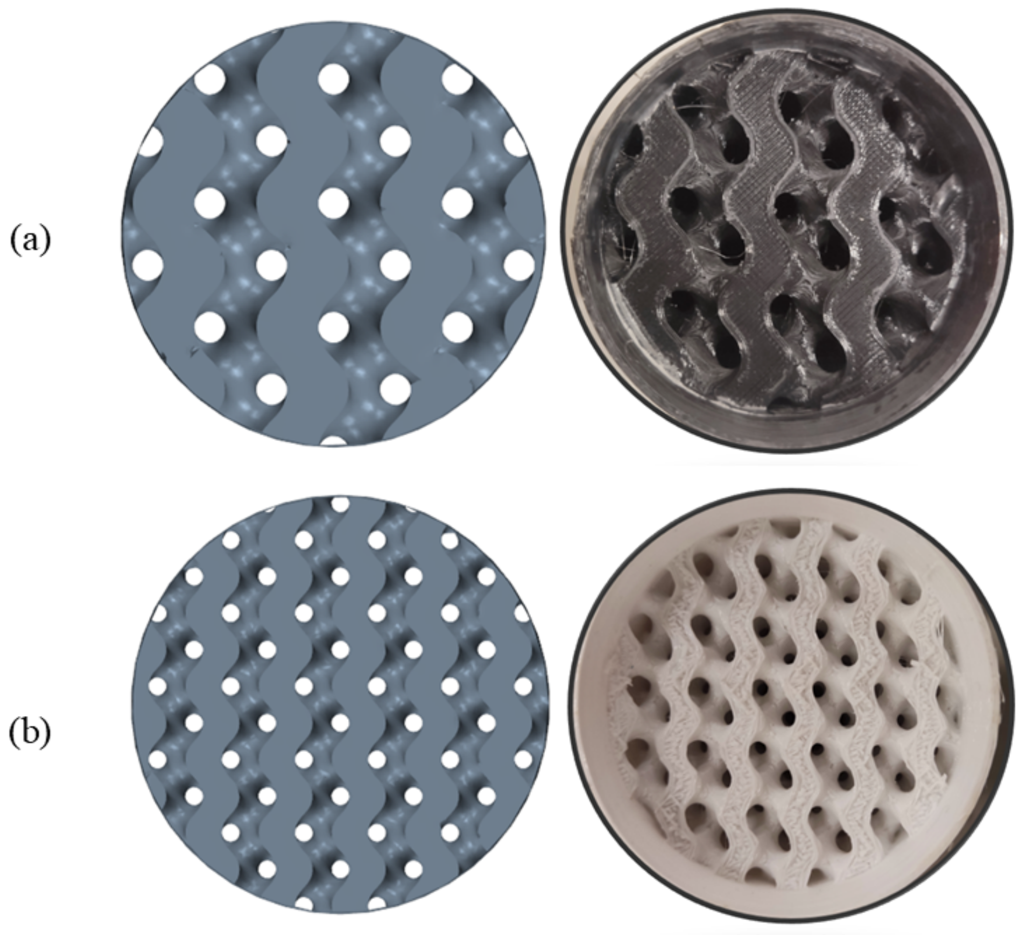

Figure 10: Comparison of printed and generated geometries-(a) Low-frequency, (b) High-frequency.

was fully developed. At the test section, two holes were located close to the TPMS gyroid structure at the inlet and outlet parts to regulate the pressure transducer's high-pressure and low-pressure sensors. The test setup passed the leakage test.

The comparison between the computer-generated geometries and the 3D-printed models reveals noticeable disparities that are important to consider when analyzing the experimental results. The digital models, as seen in Figure10 (a) and (b), exhibit smooth and continuous surfaces, which align with the theoretical design of the TPMS structures. In contrast, the 3D-printed models show evidence of surface roughness inherent to the additive manufacturing process and potential cavities or irregularities within the structures. These discrepancies can introduce additional factors influencing the fluid flow characteristics, such as increased drag or altered flow pathways. The surface roughness of the printed models, especially visible in the darker material of the higher frequency geometry, could lead to deviations in the pressure drop performance compared to the idealized digital models. Additionally, cavities within the 3D-printed structures could allow for unintended fluid retention or flow, further impacting the accuracy of the experimental validation. Therefore, these factors should be accounted for when interpreting the results, as they highlight the limitations of physical manufacturing techniques in replicating perfectly smooth and precise TPMS geometries.

CHAPTER V

RESULTS AND DISCUSSION

This section presents the numerical validation and detailed analysis of local flow and thermal transport in conjunction with the interfacial heat transfer coefficient distribution in the walls and the globally averaged heat transfer coefficient concerning the pumping power.

5.1 Experimental results

5.1.1 Fitting curve for experimental results

Ten experiments were performed on each TPMS geometry to validate the simulation results and capture the pressure drop effect through the structures. The experiments were conducted within a mass flow rate range of approximately 0 to 3.4 g/s. Using MATLAB software, a bootstrap sampling method was employed to analyze the data, generating a fitted curve for each frequency experiment with a 95% confidence interval (2.5% - 97.5%).

Figure 11 presents the pressure drop measurements across these experiments. The results reveal significant variation in the pressure drop observed for both TPMS structures. As highlighted in Figure 11, the low-frequency TPMS consistently exhibits a higher pressure drop than the high-frequency TPMS.

Moreover, the standard deviation of the fitted curves was calculated and included in the analysis to assess the reliability of the experimental results. The error bars in the figure indicate the standard deviation at various points along the fitted curve, emphasizing the variability inherent in the experimental data. Including these error bars further underscores the robustness of the data analysis, confirming that while the pressure drop in low-frequency TPMS is indeed greater, there is a degree of variability

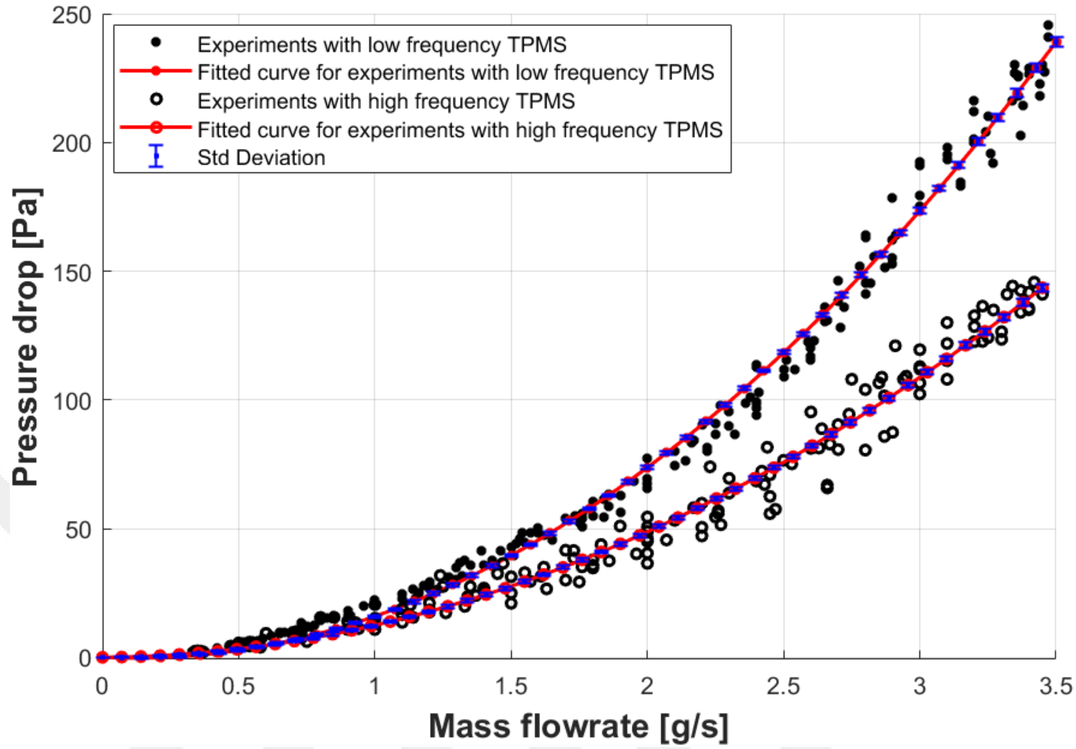

Figure 11: Pressure drop - Mass flowrate comparison.

that should be considered in interpreting the results.

5.1.2 Uncertainty analysis of experimental results

The experimental data for both low and high-frequency TPMS structures were analyzed by fitting a quadratic curve to the data points, representing the relationship between the mass flow rate and the pressure drop. The fitted curves are accompanied by upper and lower confidence interval boundaries calculated at a 68% confidence level as illustrated in Figure 12. Specifically, this approach allows us to understand the distribution of the data and confirm that 68% of the experimental data lies within these boundaries.

The 68% confidence interval was selected to correspond to ±1 standard deviation from the mean of the fitted curve. This interval suggests that, under normal distribution assumptions, approximately 68% of the experimental data points should fall within these boundaries. The fitted curves not only follow the general trend of the experimental data but also serve as a predictive tool, allowing for the estimation of pressure drop at various mass flow rates within the bounds of expected variability. The equations of the mean fitted curve and the boundaries are expressed below:

The equations of the mean fitted curve for experiments of low and high-frequency TPMS:

$$Y_{\text{low-frequency TPMS}} = 19.1991 \cdot X^2_{\text{low-frequency TPMS}} \tag{22}$$

$$Y_{\text{high-frequency TPMS}} = 11.8876 \cdot X^2_{\text{high-frequency TPMS}} \tag{23}$$

The upper and lower boundaries for the experiments of low and high-frequency TPMS structures:

$$Y_{\text{low-frequency TPMS}} = 19.1991 \pm 1.7 \cdot X^2_{\text{low-frequency TPMS}} \tag{24}$$

$$Y_{\text{high-frequency TPMS}} = 11.8876 \pm 2.2 \cdot X^2_{\text{high-frequency TPMS}} \tag{25}$$

Y represents the pressure drop, and X represents the mass flow rate.

For the low-frequency TPMS structure, the fitted quadratic curve demonstrates a strong correlation with the experimental data. Most data points reside comfortably within the 68% CI boundaries, indicating that the model effectively captures the system's behavior. The confidence intervals provide a quantitative measure of uncertainty, suggesting that the observed variations in the data are within expected limits.

Similarly, the high-frequency TPMS structure exhibits a robust relationship between the experimental data and the fitted curve. Although the data points are more dispersed than the low-frequency structure, a significant portion of the data still falls within the 68% CI boundaries. This dispersion may indicate higher sensitivity to variations in mass flow rate or inherent complexities in the high-frequency TPMS structure.

The uncertainty analysis of the experimental data, through the use of fitted curves and confidence intervals, has provided a comprehensive understanding of the pressure

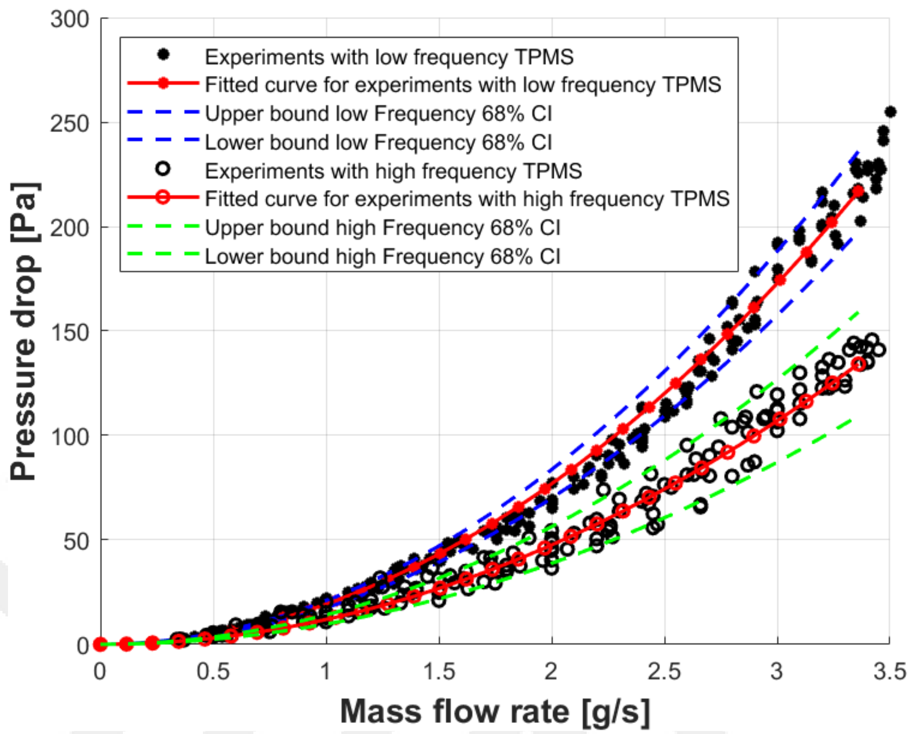

Figure 12: Percentile analysis of Pressure drop - Mass flow rate comparison.

drop behavior in TPMS structures. The 68% confidence intervals as the boundaries serve as a measure of uncertainty, ensuring that most of the experimental data align with the expected outcomes.

5.1.3 Uncertainty analysis of measuring devices

To ensure the reliability of the experimental measurements, an uncertainty analysis was conducted for the mass flow rate and pressure drop values obtained using the flow meter (VA525) and pressure transducer (ABB 2600T), respectively. This analysis considered the specific accuracies of the measuring instruments used.

The mass flow rate ($\dot{m}$) was measured using the VA525 compact inline flow meter, which operates with an accuracy of $\pm1.5\%$ of the measured value and $\pm0.3\%$ of the full-scale value. Given a measured mass flow rate of 3.36 (g/s) and full scale of 47.9 (g/s), the uncertainties of measured value and full-scale were calculated as follows:

$$U_{\dot{m},\text{measured}} = 0.015 \times 3.36 = 0.0504\,\text{g/s} \tag{26}$$

$$U_{\dot{m},\text{full scale}} = 0.003 \times 47.9 = 0.0.1437\,\text{g/s} \tag{27}$$

The total uncertainty in the mass flow rate was then determined using the root sum of squares (RSS) method:

$$U_{\dot{m}} = \sqrt{(U_{\dot{m},\text{measured}})^2 + (U_{\dot{m},\text{full scale}})^2} \approx 0.1527\,\text{g/s} \tag{28}$$

The pressure drop (ΔP) was measured using the ABB 2600T pressure transducer, which has an accuracy of $\pm 0.05\%$ of the measured value per 1 kPa. For a measured pressure drop of 219.5 Pa, the uncertainty was calculated as:

$$U_{\Delta P} = 0.0005 \times 0.2195\,\text{kPa} = 0.00010975\,\text{kPa} \approx 0.10975\,\text{Pa} \tag{29}$$

Since the mass flow rate and pressure drop are independent measurements, their uncertainties can be reported independently. The results are as follows:

$$\begin{aligned} \text{Mass Flow Rate:} &\quad 3.36 \pm 0.1527\,\text{g/s} \\ \text{Pressure Drop:} &\quad 219.5 \pm 0.10975\,\text{Pa} \end{aligned}$$

These values represent the measurement uncertainties associated with the experimental setup, ensuring the accuracy and reliability of the collected data.

5.2 RANS model results vs Experimental results

This section compares the RANS computational results with those of experimental investigations. Figure 13 shows the velocity vector field for the TPMS geometries at a mass flow rate of 2.2 (g/s). Specifically, Figure 13a depicts the fluid flow within the high-frequency TPMS structure. In contrast, the corresponding visualization of the fluid flow within the low-frequency TPMS structure is presented in Figure 13b. These

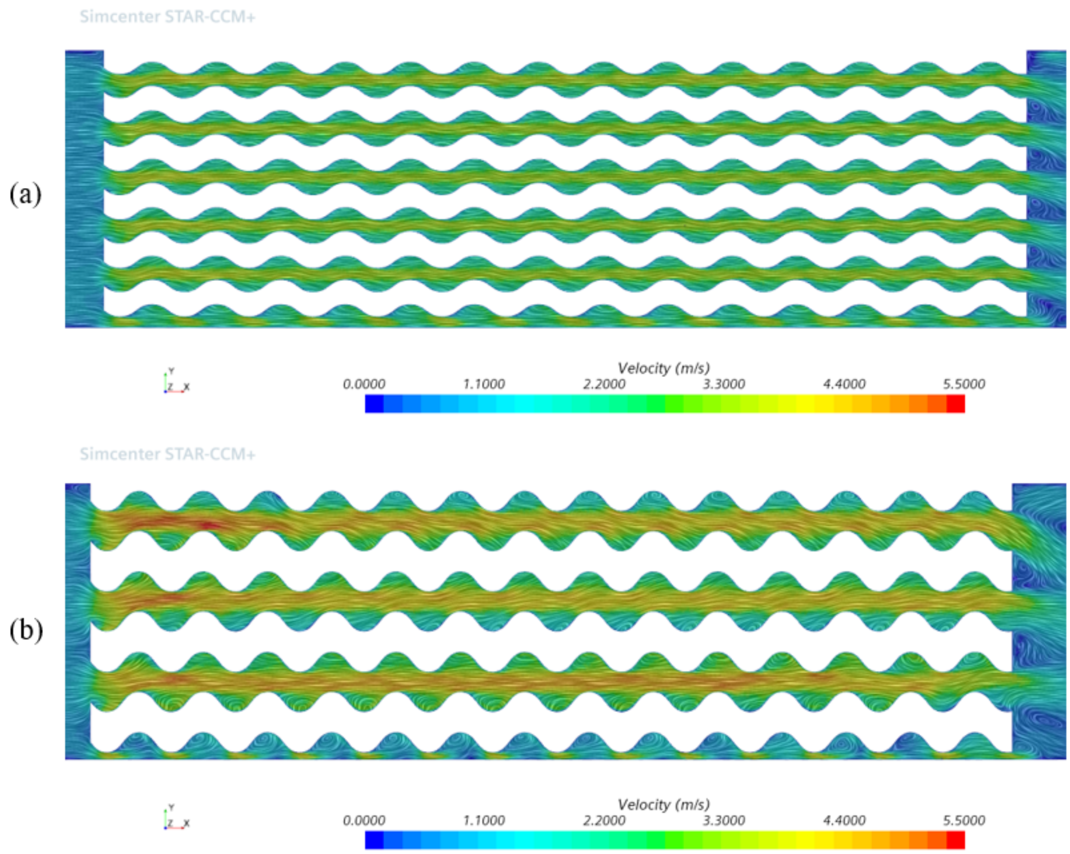

Figure 13: Velocity vector scene at a mass flow rate of 2.2 g/s - (a) for the high-frequency geometry and (b) for the low-frequency geometry.

visual representations offer insights into the spatial distribution and characteristics of fluid motion within each respective TPMS geometry. The two geometries under consideration exhibit similar characteristics, yet their curvatures differ significantly, resulting in distinct fluid-flow behaviors. In the comparative analysis of the fluid flow patterns depicted in Figure 13, it becomes evident that the vortexes are more visible in Figure 13b, which causes more energy loss.

Figure 14 presents the experimental and computational pressure drop as a function of the mass flow rate for high- and low-frequency TPMS gyroid structures. It is evident from the computational results that the low-frequency TPMS gyroid structure exhibits a higher pressure drop than that of the high-frequency counterpart. Regarding heat transfer, our computational analysis indicates that both TPMS structures

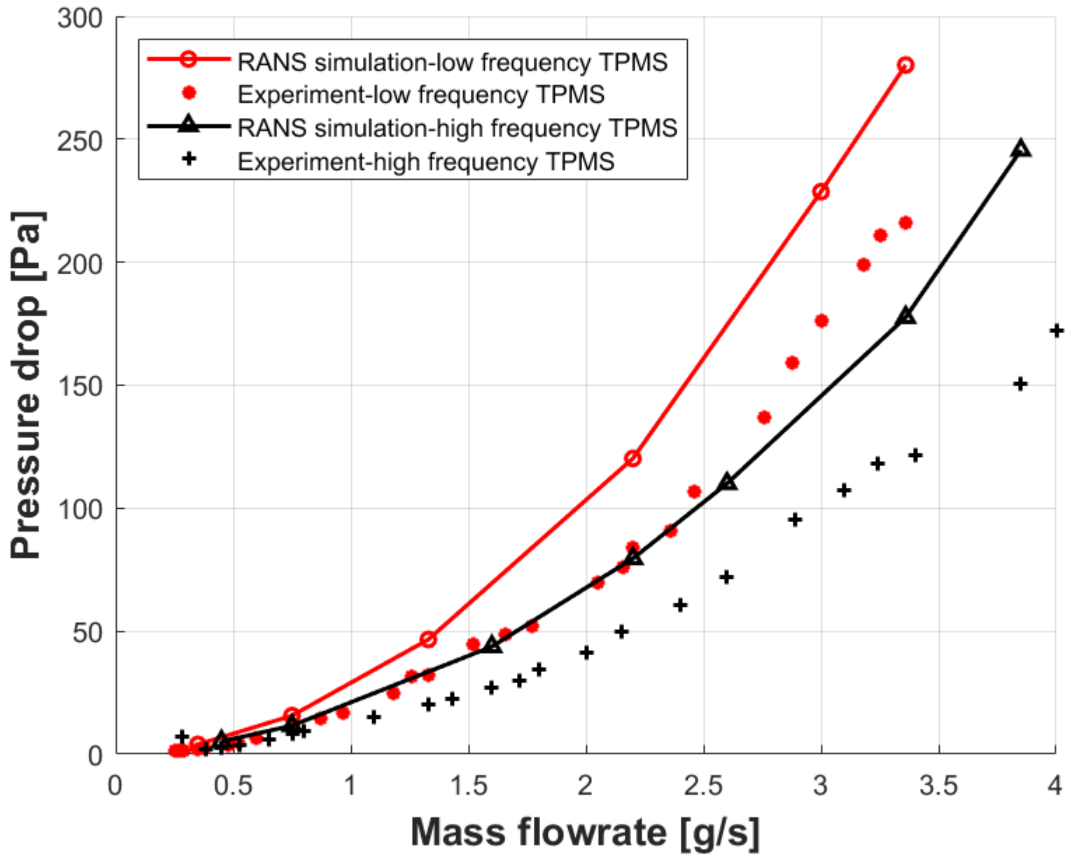

Figure 14: Mass flow rate - Pressure drop comparison.

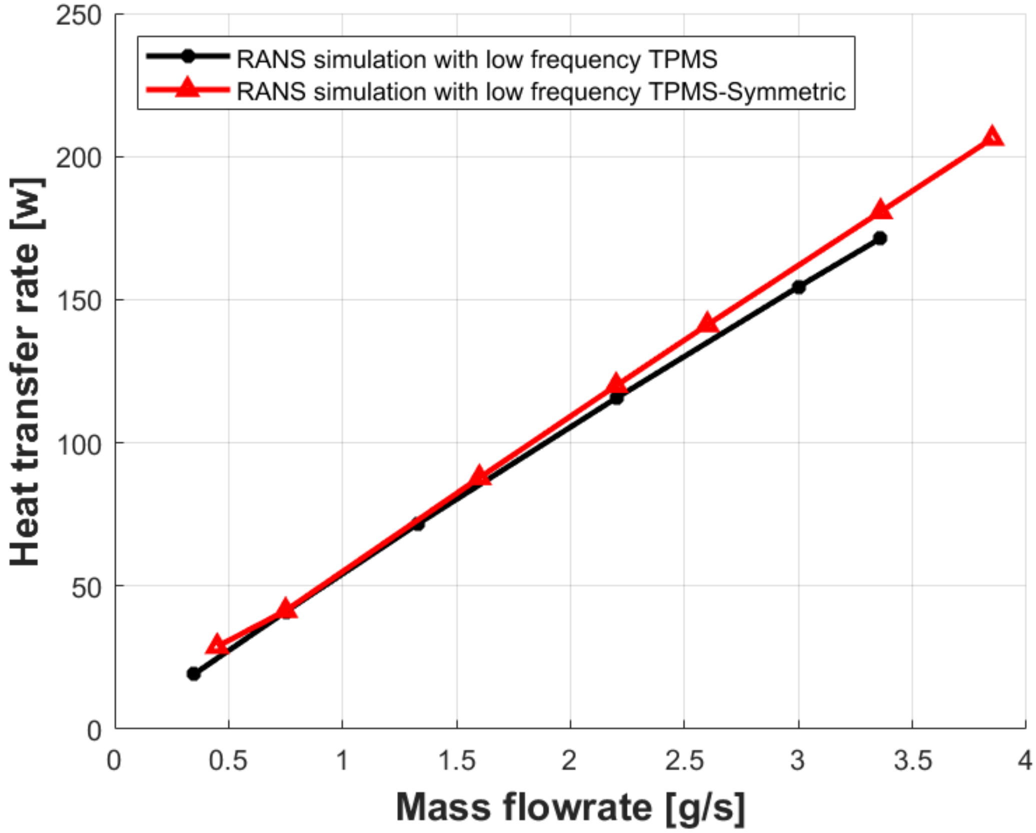

Figure 15: Mass flow rate - Heat transfer comparison.

demonstrate nearly identical heat transfer rates, as illustrated in Figure 15. This finding is noteworthy, given that the high-frequency TPMS gyroid structure has a surface area approximately 25% greater than its low-frequency counterpart. The similarity in heat transfer rates despite this disparity in surface area was unexpected and merits further investigation. Although there is a notable discrepancy between the computational and experimental results, we have successfully captured the underlying trend and thus validated our computational analysis. This suggests that although our simulations may not precisely mirror real-world observations, they effectively capture the fundamental trends and behaviors of the TPMS structures under investigation.

To better understand the underlying causes of the higher pressure drop observed in low-frequency TPMS structures, we analyzed the total energy dissipation within

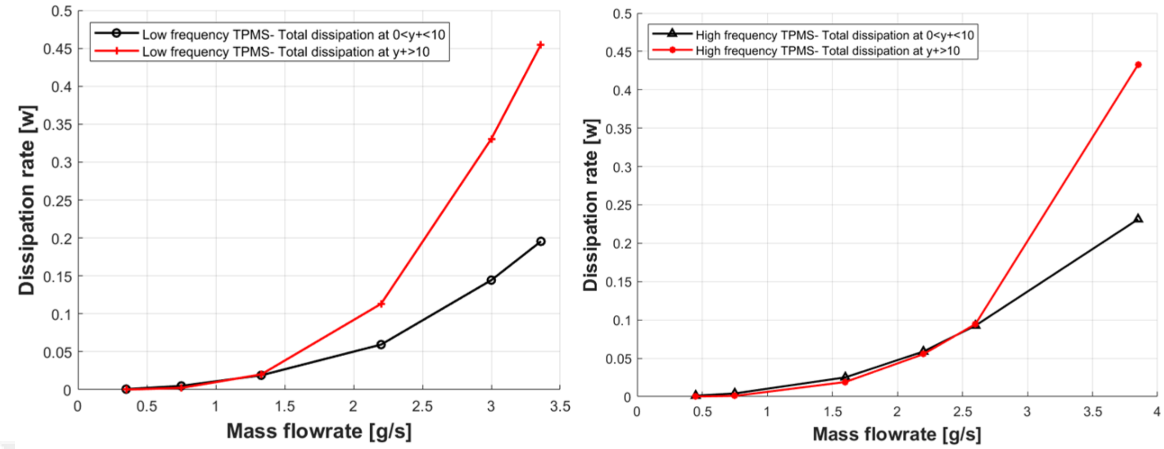

(a) (b)

Figure 16: Mass flowrate - Dissipation rate comparison - (a) Low-frequency geometry and (b) High-frequency geometry.

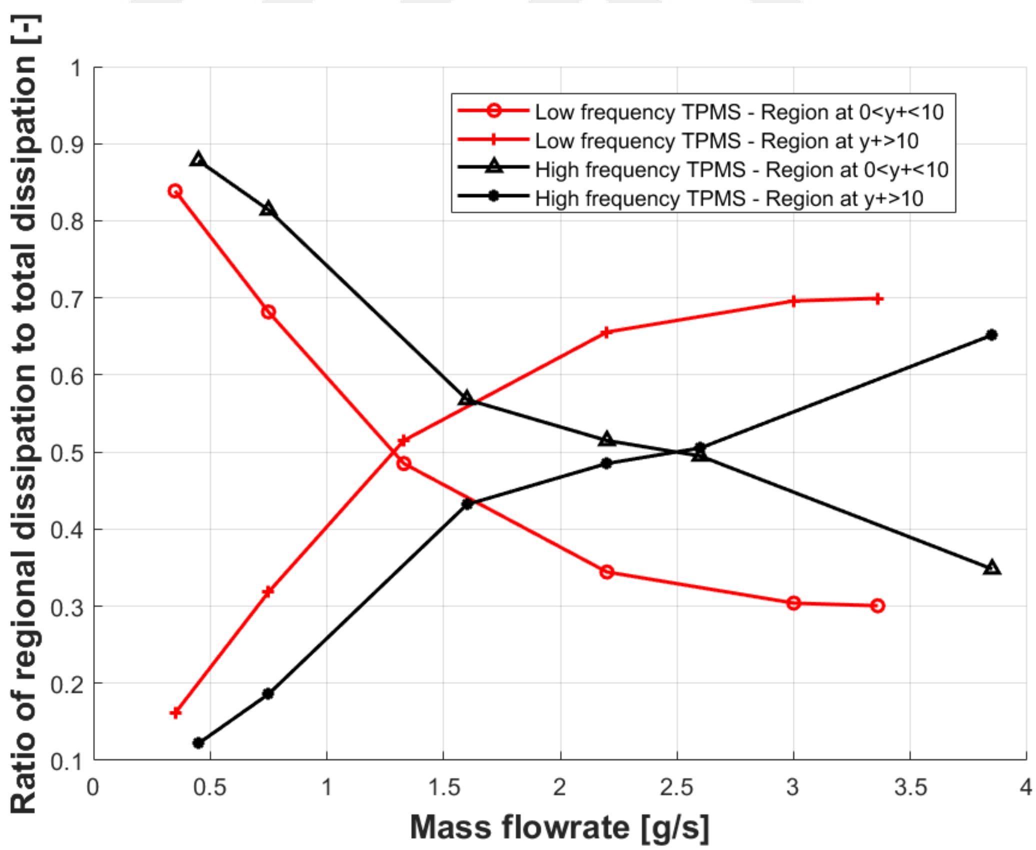

Figure 17: Mass flowrate - Ratio of regional dissipation to total Dissipation comparison.

distinct regions $0 < y^+ < 10$ and $y^+ > 10$. Mean velocity dissipation and turbulent dissipation are considered to be total dissipation. Figures 16 and 17 show the total dissipation observed within high- and low-frequency TPMS structures. Our observations reveal that, regardless of the structure type, the dissipation near the wall is marginally higher under lower mass flow rates than in regions farther away. However, this trend undergoes a notable reversal at higher mass flow rates, where dissipation at $y^+ > 10$ significantly surpasses that occurring near the wall.

5.3 LES model results vs Experimental results

This section compared the LES computational results with those of experimental investigations.

At a mass flow rate of 2.2 (g/s), Figure 18 reveals the velocity vector field for the TPMS geometries. In this regard, Figure 18b describes how fluids move in the high-frequency TPMS structure. On the other hand, Figure 18a shows visualization of fluid flowing in low-frequency TPMS structures. These visual representations provide information on how fluid moves across each particular TPMS geometry and its distribution over space, as seen from these graphics. Besides, these two geometries have similar properties, although their curvatures differ greatly, leading to distinct behaviors of fluid flows within them. Figure 18 shows that vortices are more pronounced in Figure 18a, which is reasoned to expect more energy loss.

Figure 20 illustrates the velocity components (u, v, and w) at the center of an empty volume point of the gyroid structure located 15.4 cm downstream within the channel of a TPMS structure. The exact location of the points is demonstrated by figure 19, which (a) is for low-frequency, and (b) is for high-frequency TPMS. This analysis captures the turbulent effects in low- and high-frequency TPMS structures by measuring the velocity components at this critical location. Subfigure (a) represents the u component, subfigure (b) the v component, and subfigure (c) the w

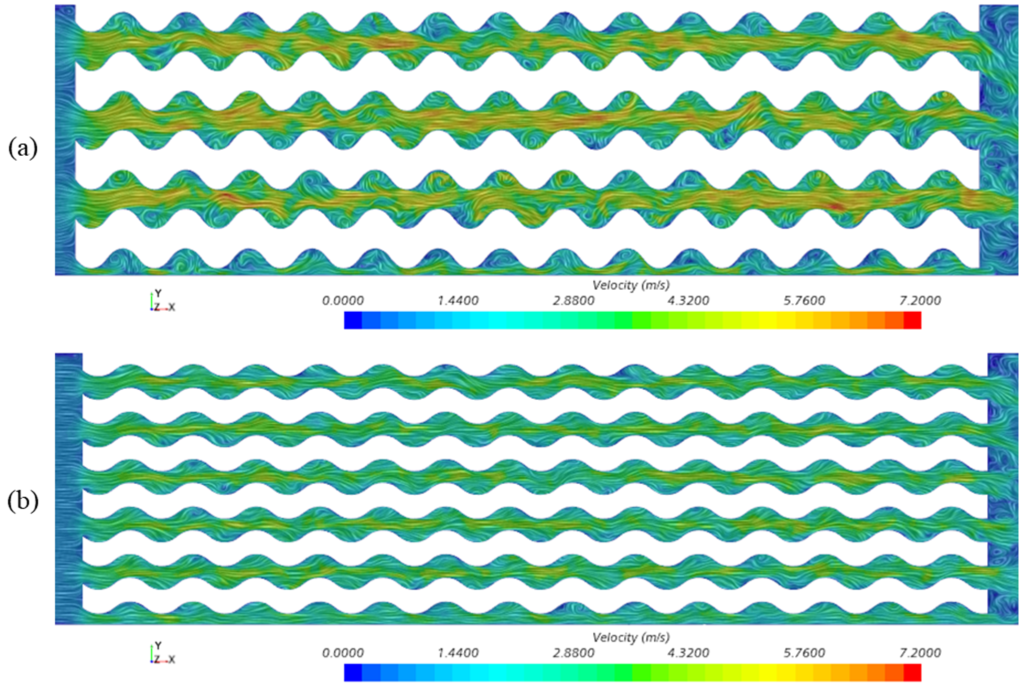

Figure 18: Velocity vector scene at a mass flow rate of 2.2 (g/s) - (a) Low-frequency geometry, (b) High-frequency geometry.

component. The data indicate that the low-frequency TPMS structure exhibits significantly greater variation in velocity signals than the high-frequency TPMS structure in all components. This pronounced variability suggests a higher level of turbulence within the low-frequency TPMS, as turbulent flow typically manifests through fluctuating velocity signals. In contrast, the high-frequency TPMS structure demonstrates relatively stable velocity signals, indicating less turbulence. These findings underscore the importance of TPMS frequency in influencing the turbulence characteristics within the fluid channels.

In Figure 21, we demonstrate the experimental and computational pressure drop as a function of the mass flow rate for high- and low-frequency TPMS gyroid structures. It is evident from the computational results that the low-frequency TPMS gyroid structure exhibits a higher pressure drop than that of the high-frequency counterpart. In addition, in Figure 21, it can be observed that the numerical results are higher than the experimental investigations. This discrepancy can be attributed to cavities

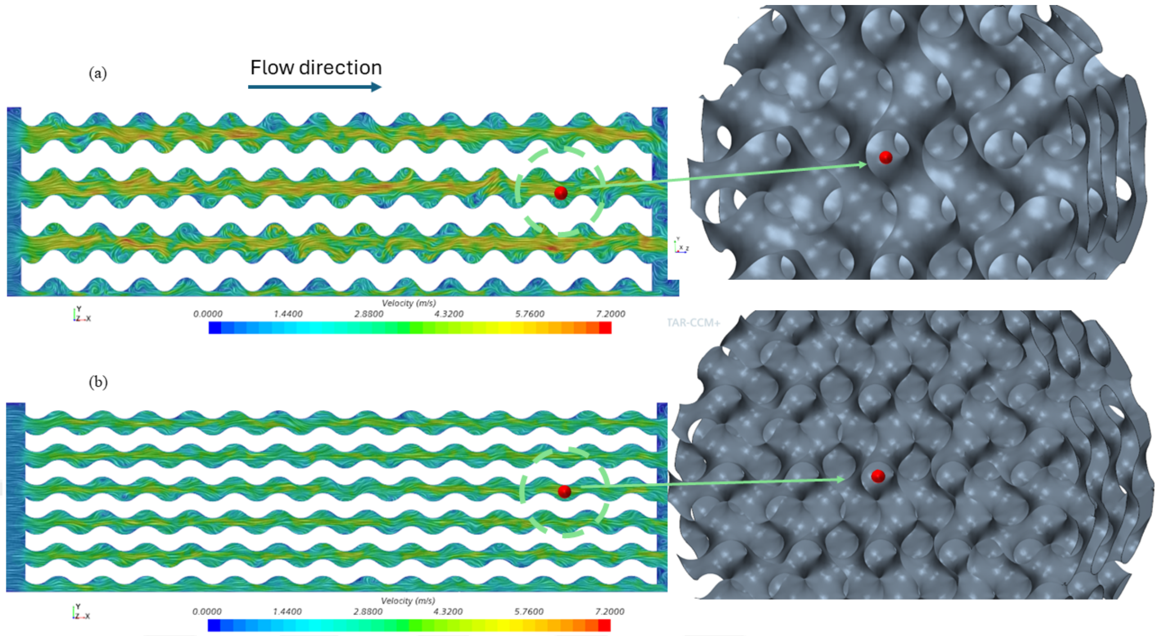

Figure 19: Cross-sectional view of the location of the points inside the TPMS structure - (a) Low-frequency TPMS, (b) High-frequency TPMS.

caused by the quality of the 3d printed structures. Some cavities were observed on the printed gyroid structures. These cavities allow air to flow through the interconnected voids rather than exclusively through the intended channels of the TPMS structures, resulting in faster airflow through the TPMS structure. Accordingly, we observe a higher pressure drop in numerical analysis than in real-life investigations.

In our computational heat transfer analysis, we observed that both high- and low-frequency TPMS gyroid structures exhibit nearly identical heat transfer rates, as depicted in Figure 22. This finding is particularly significant given that the high-frequency TPMS gyroid structure has a surface area approximately 25% higher than its low-frequency counterpart. Despite this substantial difference in surface area, the similarity in heat transfer rates was unanticipated and warrants further investigation. The observed phenomenon can be attributed to the fluid saturation after fully developing within the gyroid structure. The fluid heats uniformly in both geometries as constant temperature is maintained on the TPMS walls. Consequently, we measured the average surface temperature of the fluid at various sections within the fluid

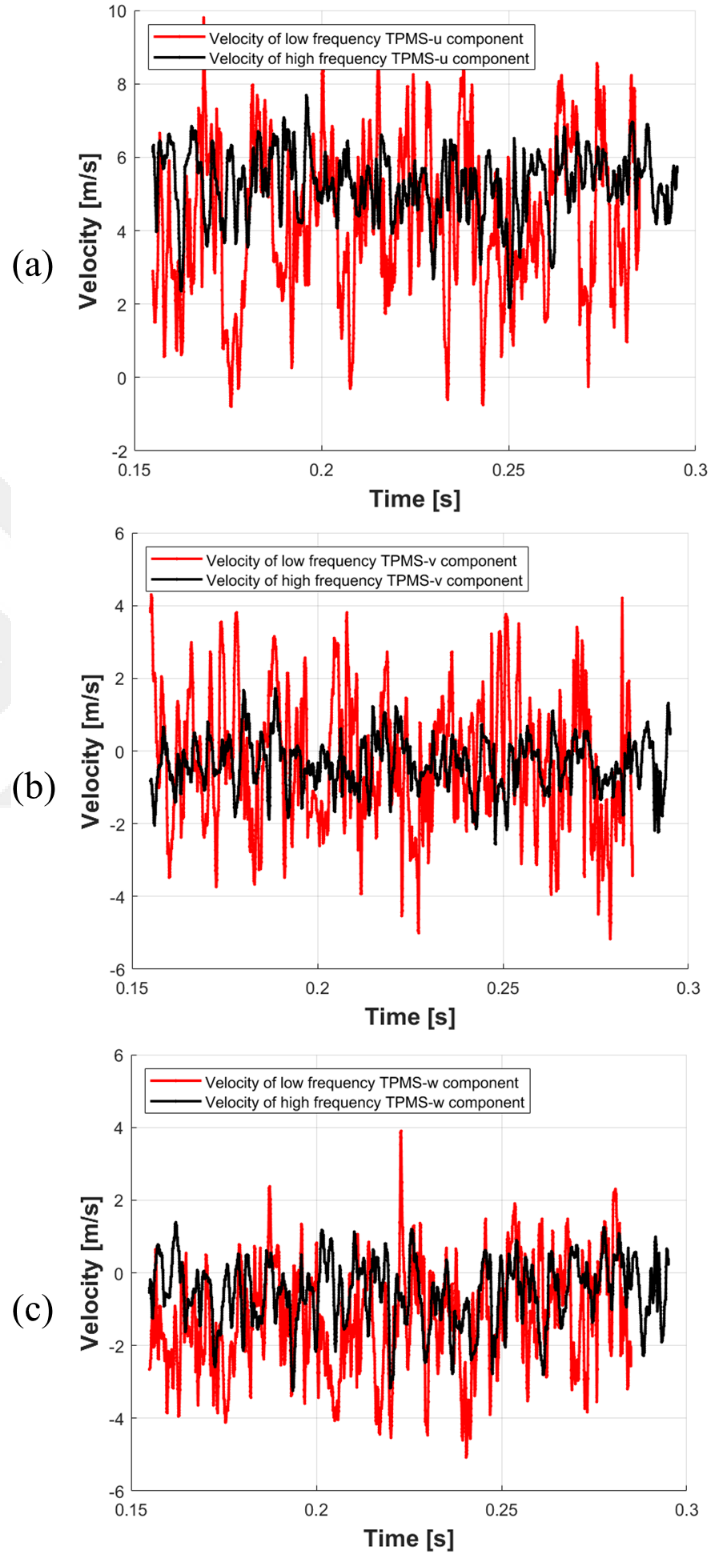

Figure 20: Instantaneous velocity data at the center of fluid volume in TPMS structure.

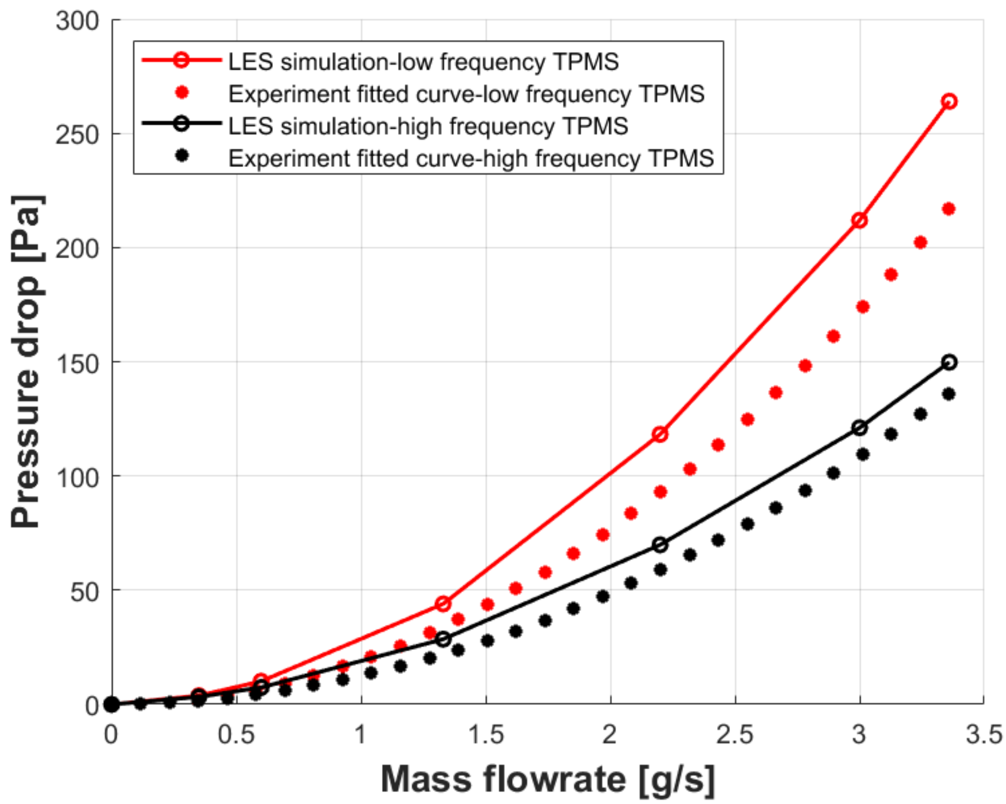

Figure 21: Mass flow rate - pressure drop comparison.

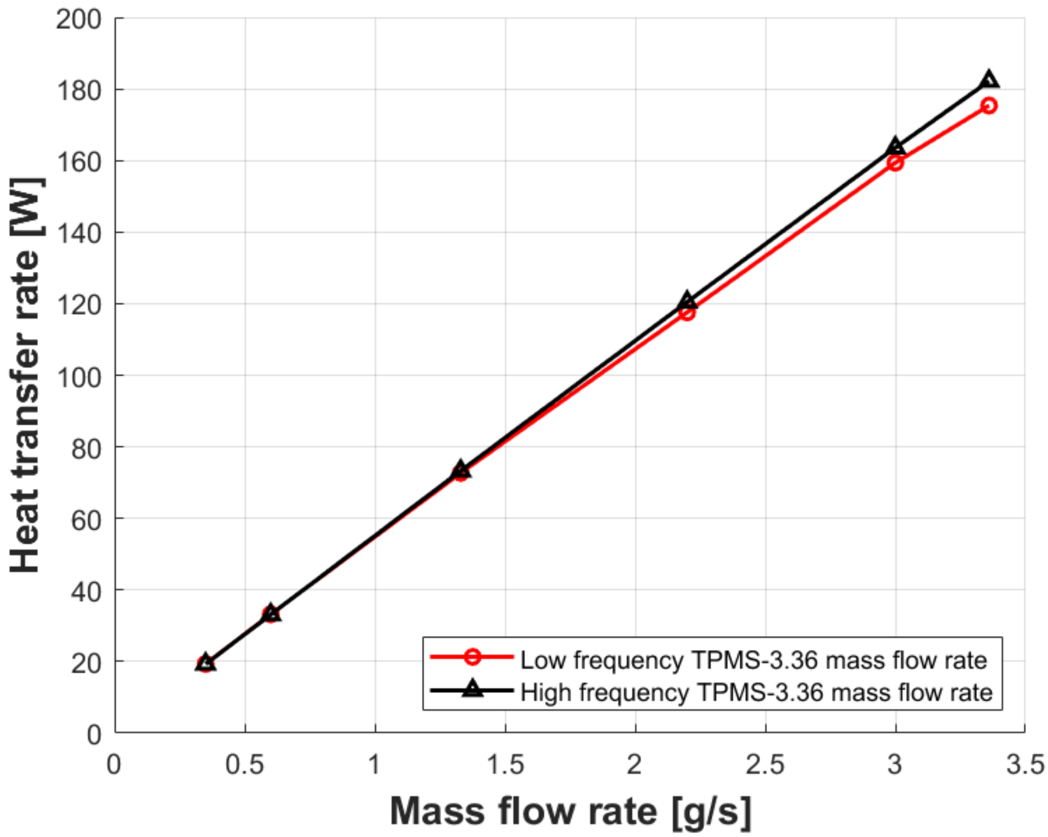

Figure 22: Mass flow rate - heat transfer rate comparison.

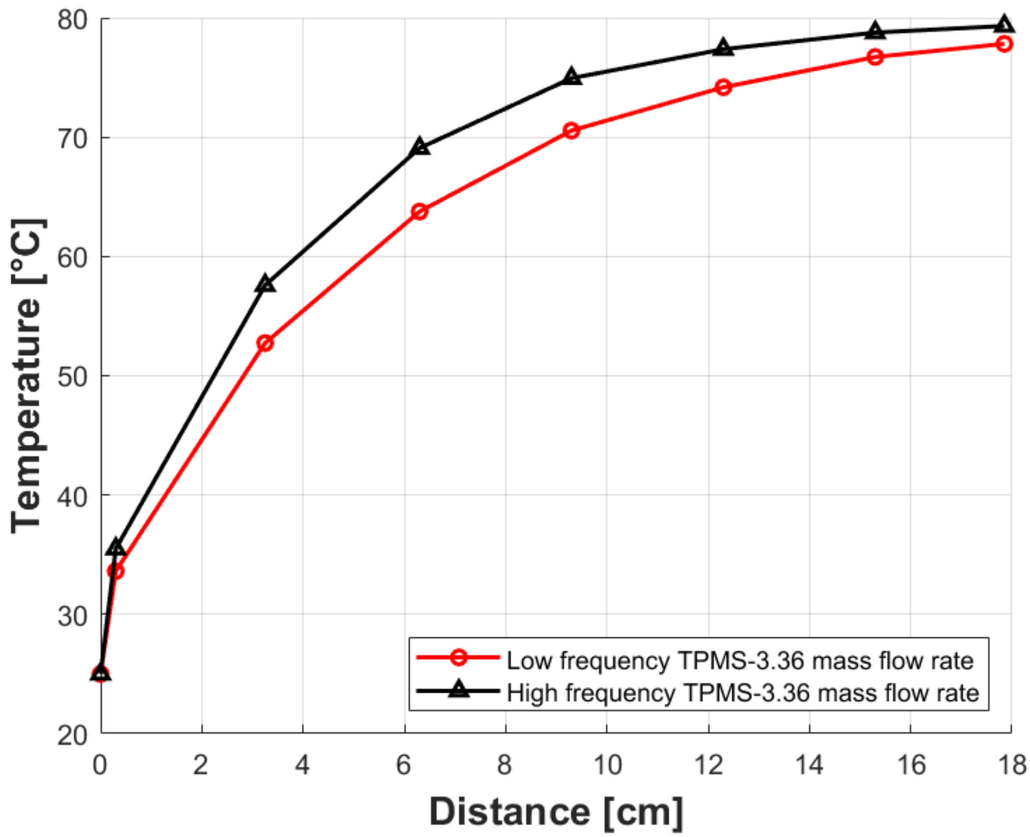

Figure 23: Fluid average temperature in various sections through the TPMS structure at 3.36 (g/s) mass flow rate.

through the gyroid structure. As illustrated in Figure 23, the data reveals that the high-frequency gyroid structure, owing to its greater surface area, results in a higher average temperature of the fluid than the low-frequency structure at a mass flow rate of 3.36 (g/s). This detailed temperature profile underscores the intricate interplay between surface area and heat transfer rates in TPMS structures. While the high-frequency gyroid has a larger surface area, which theoretically should enhance heat transfer, the nearly identical heat transfer rates between the two structures suggest that the fluid reaches a thermal equilibrium state within the gyroid structure, thereby minimizing the expected advantages of a larger surface area. This equilibrium is likely due to the fluid being fully developed and the heat transfer being governed by the conductive and convective properties of the fluid rather than merely the surface area.

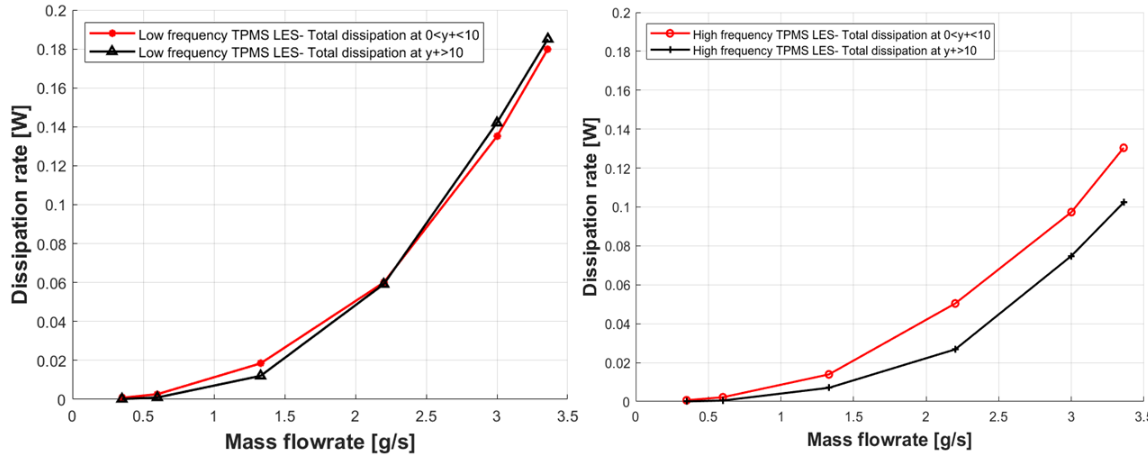

(a) (b)

Figure 24: Mass flowrate - Dissipation rate comparison - (a) Low-frequency geometry and (b) High-frequency geometry.

Although there is a notable discrepancy between the computational and experimental results, we have successfully captured the underlying trend and thus validated our computational analysis. This suggests that although our simulations may not precisely mirror real-world observations, they effectively capture the fundamental trends and behaviors of the TPMS structures under investigation.

To validate our pressure drop results and investigate the reasons for the higher pressure drop in low-frequency TPMS, we analyzed the total energy dissipation during fluid flow within porous media across different regions $0 < y+ < 10$ and $y+ > 10$. SGS dissipation and turbulent dissipation are considered to be total dissipation. Figures 24 and 25 show the total dissipation observed within high- and low-frequency TPMS structures. Our observations reveal that, regardless of the structure type, the dissipation near the wall is marginally higher under lower mass flow rates than in regions farther away. However, this trend undergoes a notable reversal at higher mass flow rates, where dissipation at $y+ > 10$ significantly surpasses that occurring near the wall. Figure 24 demonstrates that energy dissipation is significantly greater in low-frequency TPMS compared to high-frequency TPMS. This increased dissipation can be attributed to the more pronounced turbulence structures in the low-frequency

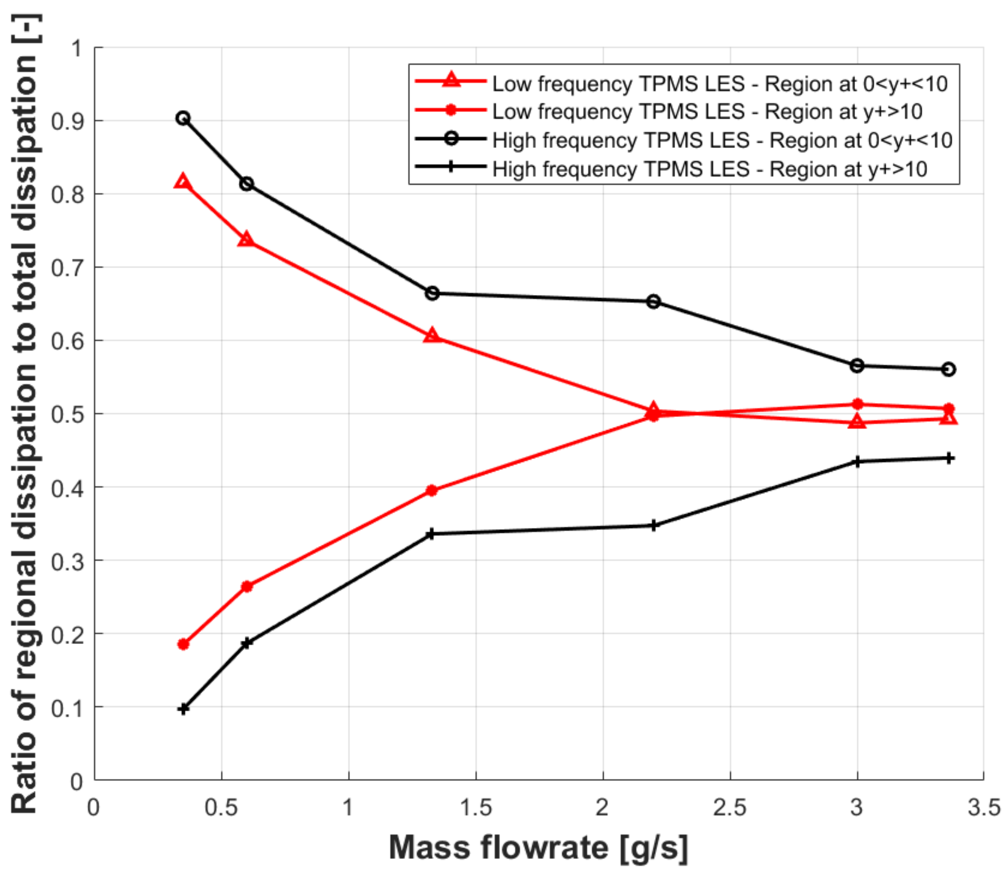

Figure 25: Mass flowrate - Ratio of regional dissipation to total Dissipation comparison.

TPMS. These turbulent structures contribute to higher energy losses, resulting in the observed disparity in dissipation between the two geometries.

5.3.1 Symmetrically located TPMS results

In our analysis of the turbulent kinetic energy within the TPMS structures, as illustrated in Figure 27, we observed variability in the turbulent kinetic energy across different channels. This non-uniform distribution of turbulent kinetic energy suggests that the flow may not be fully developed throughout the TPMS structure, which could contribute to an overestimation of the simulation results. To address this issue, we conducted an additional analysis by placing symmetrically located TPMS structures inside a cylindrical domain.

The cross-sectional view of the symmetrically and asymmetrically located TPMS geometries inside the cylinder are demonstrated in Figure 26. In the (a) and (b) geometries in Figure 26, The channels of the TPMS structures are asymmetrically located within the cylinder. This means that the pattern of the channels doesn't mirror itself evenly across the axes. The asymmetry in these configurations could influence the flow characteristics through these structures, leading to a non-uniform distribution of flow resistance or pressure drop across the geometry. In contrast, in the (c) and (d) geometries, the channels of the TPMS structures are symmetrically located within the cylinder. This symmetric arrangement suggests that the flow would encounter a more uniform resistance, potentially leading to a more consistent pressure drop or fluid flow pattern across the geometry. The green and orange lines represent the primary axes (x, y, and z), clearly referencing the orientation in each case.

Figure 27 illustrates the distribution of turbulent kinetic energy in low-frequency and high-frequency TPMS structures at a mass flow rate of 2.2 g/s, as obtained from RANS simulations. The results indicate that the non-uniformity in turbulent kinetic energy distribution may be a significant factor influencing the accuracy of the

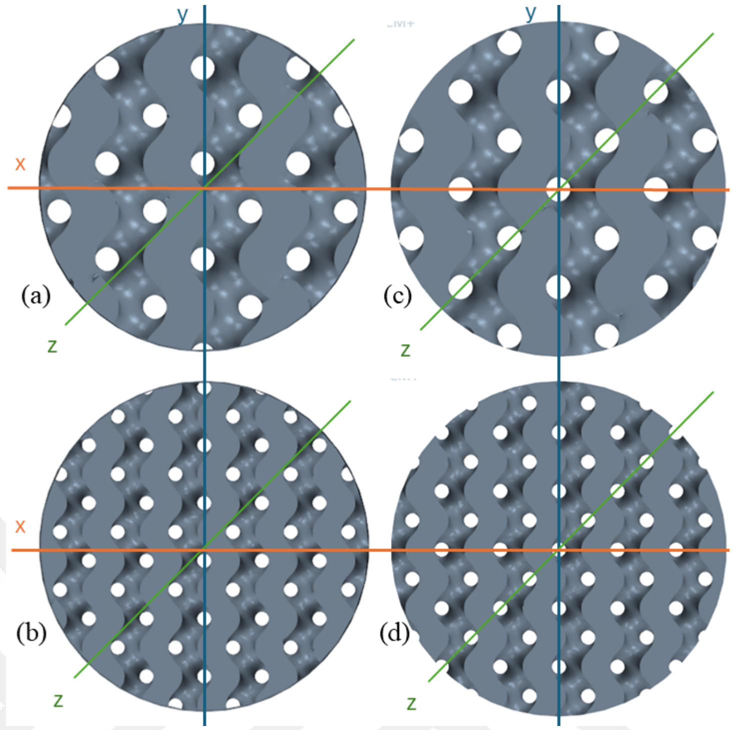

Figure 26: Comparison of Symmetrically and asymmetrically located TPMS geometries inside the cylinder - (a) and (b) asymmetrical, (c) and (d) symmetrical .

simulation outcomes.

To further investigate the impact of symmetrical positioning on flow development and energy dissipation, we performed a symmetric analysis of the TPMS structures at the critical and highest mass flow rate of 3.36 g/s using the RANS model. The turbulent kinetic energy distributions in low-frequency and high-frequency TPMS structures under these conditions are depicted in Figure 28. This analysis provides a more comprehensive understanding of how symmetrical placement influences the flow characteristics and overall performance of TPMS structures in high-mass-flow-rate scenarios. As illustrated in Figure 28, the distribution of the turbulent kinetic energy is uniform in symmetrically located TPMS structures rather than asymmetrical ones.

Figure 29 presents the relationship between mass flow rate and pressure drop for both LES and RANS models, alongside the results for symmetrically located TPMS structures. The analysis reveals that LES simulations yield more accurate predictions

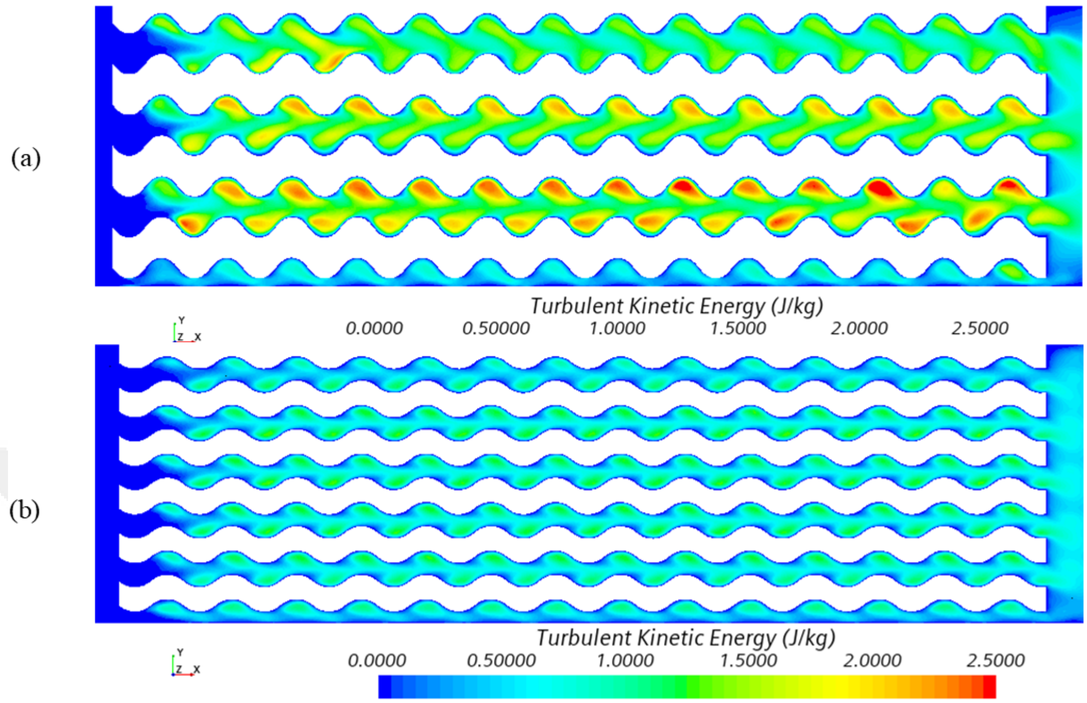

Figure 27: RANS turbulent kinetic energy scene at 2.2 (g/s) mass flow rate - (a) Low-frequency TPMS, (b) High-frequency TPMS.

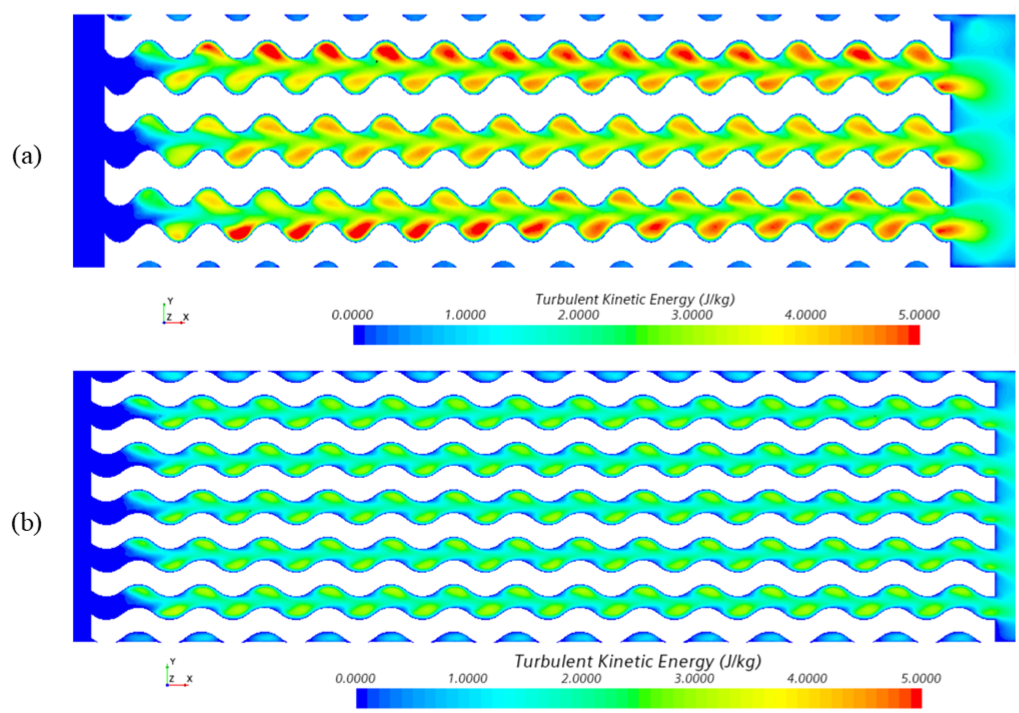

Figure 28: RANS turbulent kinetic energy scene of symmetrically located TPMS at 3.36 (g/s) mass flow rate - (a) Low-frequency TPMS, (b) High-frequency TPMS.

for high-frequency TPMS structures than the RANS model, particularly at higher mass flow rates. This suggests that LES is better suited for capturing the intricate turbulence dynamics within these geometries.

However, a notable discrepancy exists between LES predictions and experimental data for low-frequency TPMS structures. This disparity can be attributed to the more intense and complex turbulent structures observed in the low-frequency TPMS, which are challenging to capture accurately even with LES.

Moreover, the pressure drop observed in the symmetrically located TPMS structures in RANS simulations was higher than the experimental results. This is an intriguing finding, as it might suggest that while symmetrical alignment of TPMS structures can lead to a more uniform distribution of turbulent kinetic energy, it does not necessarily translate into a reduced pressure drop. The uniform distribution of turbulent kinetic energy in the symmetrically located TPMS structures results in a lower pressure drop than in the asymmetrically located structures. Yet, it remains higher than the experimental observations. This highlights the complexity of flow dynamics in these structures and suggests that further refinement in modeling approaches or structural design might be necessary to better align with experimental data.

For the symmetrically located TPMS, the LES simulation consistently predicts lower pressure drops than those observed in the RANS at a mass flow rate of 3.36 (g/s). However, it is worth noting that the LES results are almost identical to the experimental pressure drop at a mass flow rate of 3.36 g/s. This indicates that the LES result at the critical mass flow rate for the low-frequency TPMS structure aligns well with experimental data, reflecting its potential accuracy in predicting flow characteristics under certain conditions.

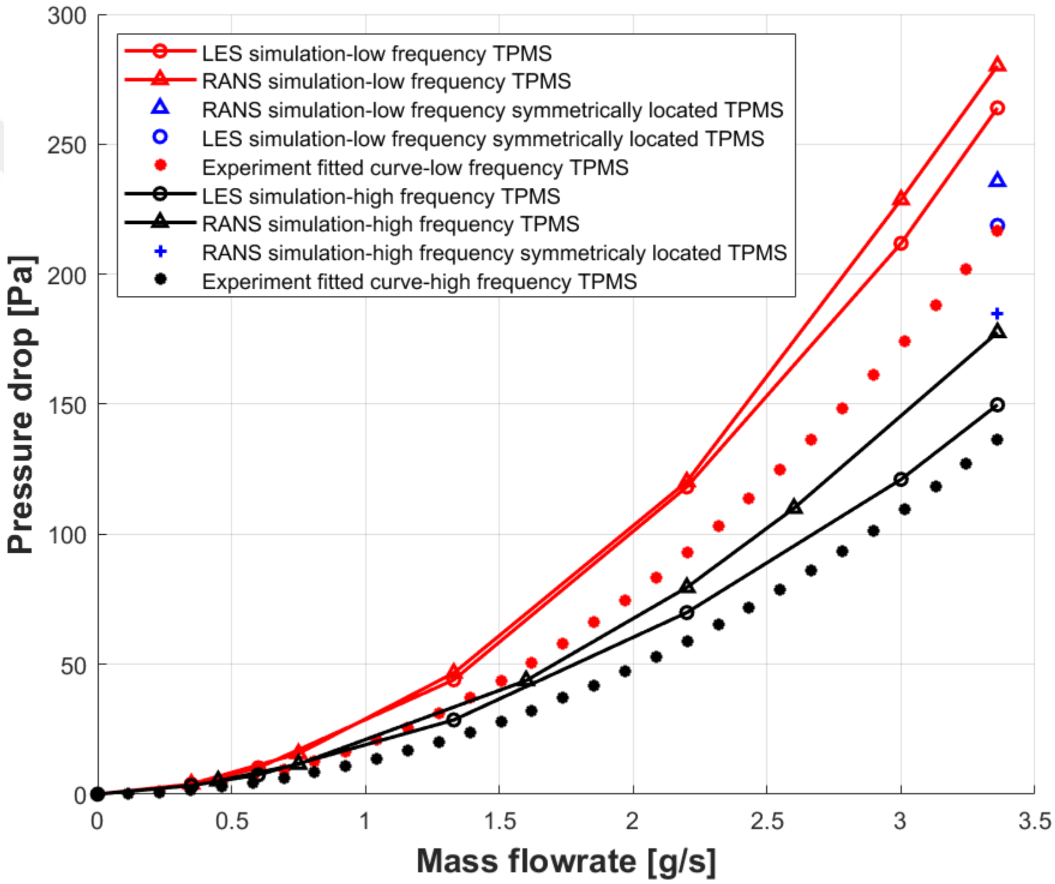

Figure 29: Mass flow rate - pressure drop comparison of symmetrical and asymmetrical located TPMS.

CHAPTER VI

CONCLUSIONS

A comprehensive numerical and experimental investigation of the flow and heat transfer characteristics of gyroid TPMS structures was performed for input airflow mass flow rates ranging from 0.35 to 3.36 g/s, using both low- and high-frequency geometries. The study utilized two computational approaches, RANS and LES models, to accurately capture these structures' heat transfer and flow characteristics. The LES model demonstrated greater accuracy than the RANS model, particularly in high-frequency TPMS structures, where the turbulent dynamics were more effectively resolved.

- Despite the differences between numerical and experimental results, the LES simulations exhibited a consistent trend with experimental data. However, the LES model was more accurate in predicting the pressure drop and heat transfer characteristics in high-frequency TPMS structures.

- The pressure drop in high-frequency TPMS structures was lower than that in low-frequency TPMS structures, attributed to the reduced turbulent structures in high-frequency geometries. This lower pressure drop and a higher surface area resulted in more efficient heat transfer within the high-frequency TPMS structures.

- The numerical analysis predicted a higher pressure drop than the experimental results, primarily due to manufacturing imperfections in the 3D-printed TPMS structures. These imperfections, such as cavities within the printed geometries, facilitated unintended airflow pathways, significantly influencing the pressure drop measurements and causing discrepancies between the simulations and experimental data. In other words, the fluid leakage into the TPMS structure reduces the flow speed through the test section.

- Observations of turbulent kinetic energy distribution within the TPMS structures revealed that the low-frequency TPMS exhibited more intense turbulent structures, leading to higher energy dissipation. In contrast, the high-frequency TPMS displayed a more uniform distribution of turbulent kinetic energy, contributing to its lower pressure drop.

- In symmetrical TPMS structures, the uniformly distributed turbulent kinetic energy resulted in a lower pressure drop than in asymmetrical structures. However, the pressure drop in symmetrical TPMS structures was still higher than the experimental results, which could be attributed to the quality of the 3D-printed construction. This underscores the complexity of the flow dynamics and the need for further refinement in both modeling approaches and manufacturing precision.

- The average temperature within the fluid was higher in the high-frequency TPMS structure due to its 25% greater surface area than the low-frequency TPMS structure. This led to more efficient heat transfer, although the overall heat transfer rates between the two geometries remained similar due to flow saturation after the fluid was fully developed.

- The findings underscore the importance of considering manufacturing quality and its effects on validating computational models against experimental data. Further research is needed to improve the 3D printing process and account for these imperfections in simulations to achieve more accurate and reliable results.

- Contrary to conventional assumptions, the reduction in pressure drop did not result in a corresponding decrease in heat transfer rate. This observation highlights the need for a deeper investigation into the flow and heat transfer phenomena within TPMS structures and the potential for optimizing their design for enhanced performance.

- Future research should focus on refining the numerical models and improving the manufacturing process to reduce discrepancies between simulation and experimental results, thereby enhancing the fidelity of predictions and advancing the application of TPMS structures in heat exchanger technologies.

REFERENCES

[1] N. Baobaid, M. I. Ali, K. A. Khan, and R. K. A. Al-Rub, "Fluid flow and heat transfer of porous tpms architected heat sinks in free convection environment," *Case Studies in Thermal Engineering*, vol. 33, 5 2022.

[2] M. Modrek, A. Viswanath, K. A. Khan, M. I. Ali, and R. K. A. Al-Rub, "An optimization case study to design additively manufacturable porous heat sinks based on triply periodic minimal surface (tpms) lattices," *Case Studies in Thermal Engineering*, vol. 36, 8 2022.

[3] A. P. Castro, J. Santos, T. Pires, and P. R. Fernandes, "Micromechanical behavior of tpms scaffolds for bone tissue engineering," *Macromolecular Materials and Engineering*, vol. 305, 12 2020.

[4] J. Shi, L. Zhu, L. Li, Z. Li, J. Yang, and X. Wang, "A tpms-based method for modeling porous scaffolds for bionic bone tissue engineering," *Scientific Reports*, vol. 8, 12 2018.

[5] Z. Chen, B. Wu, X. Chen, and Y. M. Xie, "Energy absorption and impact resistance of hybrid triply periodic minimal surface (tpms) sheet-based structures," *Materials Today Communications*, vol. 37, 12 2023.

[6] C. Zhang, H. Qiao, L. Yang, W. Ouyang, T. He, B. Liu, X. Chen, N. Wang, and C. Yan, "Vibration characteristics of additive manufactured iwp-type tpms lattice structures," *Composite Structures*, vol. 327, 1 2024.

[7] T. Femmer, A. J. Kuehne, and M. Wessling, "Estimation of the structure dependent performance of 3-d rapid prototyped membranes," *Chemical Engineering Journal*, vol. 273, pp. 438–445, 8 2015.

[8] F. Hesselmann, N. Scherenberg, P. Bongartz, S. Djeljadini, M. Wessling, C. Cornelissen, T. Schmitz-Rode, U. Steinseifer, S. V. Jansen, and J. Arens, "Structure-dependent gas transfer performance of 3d-membranes for artificial membrane lungs," *Journal of Membrane Science*, vol. 634, 9 2021.

[9] A. Ghahremannezhad and K. Vafai, "Thermal and hydraulic performance enhancement of microchannel heat sinks utilizing porous substrates," *International Journal of Heat and Mass Transfer*, vol. 122, pp. 1313–1326, 7 2018.

[10] P. Qian, J. Wang, Z. Wu, J. Yang, and Q. Wang, "Performance comparison of methane steam reforming in a randomly packed bed and a grille-sphere composite packed bed," *Energy Conversion and Management*, vol. 193, pp. 39–51, 8 2019.

[11] Y. Q. Liu, P. X. Jiang, S. S. Jin, and J. G. Sun, "Transpiration cooling of a nose cone by various foreign gases," *International Journal of Heat and Mass Transfer*, vol. 53, pp. 5364–5372, 11 2010.

[12] G. Huang, Z. Min, L. Yang, P. X. Jiang, and M. Chyu, "Transpiration cooling for additive manufactured porous plates with partition walls," *International Journal of Heat and Mass Transfer*, vol. 124, pp. 1076–1087, 9 2018.

[13] J. Iyer, T. Moore, D. Nguyen, P. Roy, and J. Stolaroff, "Heat transfer and pressure drop characteristics of heat exchangers based on triply periodic minimal and periodic nodal surfaces," *Applied Thermal Engineering*, vol. 209, 6 2022.

[14] M. M. Moradmand and A. Sohankar, "Numerical and experimental investigations on the thermal-hydraulic performance of heat exchangers with schwarz-p and gyroid structures," *International Journal of Thermal Sciences*, vol. 197, 3 2024.

[15] D. Ansari and C. Duwig, "A gyroid tpms heat sink for electronic cooling," *Energy Conversion and Management*, vol. 319, p. 118918, 11 2024.

[16] J. W. Lee, S. H. Oh, E. Jeon, J. Kim, and K. Park, "Functional gradation of the morphological properties of tpms channel for enhanced flow performance," *Materials and Design*, vol. 224, 12 2022.

[17] M. Alteneiji, M. I. Ali, K. A. Khan, and R. K. Al-Rub, "Heat transfer effectiveness characteristics maps for additively manufactured tpms compact heat exchangers," *Energy Storage and Saving*, vol. 1, pp. 153–161, 9 2022.

[18] M. Khalil, M. I. H. Ali, K. A. Khan, and R. A. Al-Rub, "Forced convection heat transfer in heat sinks with topologies based on triply periodic minimal surfaces," *Case Studies in Thermal Engineering*, vol. 38, 10 2022.

[19] M. I. H. Ali, O. Al-Ketan, N. Baobaid, K. Khan, and R. K. A. Al-Rub, "A study on the fluid flow and heat transfer for a porous architected heat sink using the idea of cfd modelling," vol. 8, American Society of Mechanical Engineers (ASME), 2019.

[20] A. Zimmer, J. D. PachecoAraújo, K. A. Andreassen, and C. A. Grande, "Effect of manufacturing techniques in pressure drop on triple periodical minimal surface packings," *Chemie-Ingenieur-Technik*, vol. 93, pp. 967–973, 6 2021.

[21] A. Barakat, Y. Pan, and B. Sun, "Comparative heat transfer performance of tpms structures: Spotlight on fisch koch s versus gyroid, diamond and splitp lattices," *E3S Web of Conferences*, vol. 560, p. 01009, 8 2024.

[22] J. Liu, D. Cheng, K. Oo, T. L. McCrimmon, and S. Bai, "Design and additive manufacturing of tpms heat exchangers," *Applied Sciences (Switzerland)*, vol. 14, 5 2024.

[23] J. Feng, J. Fu, X. Yao, and Y. He, "Triply periodic minimal surface (tpms) porous structures: From multi-scale design, precise additive manufacturing to multidisciplinary applications," 6 2022.

[24] P. J. Gandy, S. Bardhan, A. L. Mackay, and J. Klinowski, "Nodal surface approximations to the p, g, d and i-wp triply periodic minimal surfaces," *Chemical Physics Letters*, vol. 336, pp. 187–195, 3 2001.

[25] T. J. Craft, A. V. Gerasimov, H. Iacovides, and B. E. Launder, "Progress in the generalization of wall-function treatments."

[26] Siemens, "Siemens digital industries software. simcenter star-ccm+, version 2020.03, siemens 2020. available at: https://docs.sw.siemens.com/en-us/doc/226870983/pl20230724207774020.starccmp-userguide-html?audience=external. (accessed: 02 april 2024).," 2020.

[27] F. Nicoud and F. Ducros, "Subgrid-scale stress modelling based on the square of the velocity gradient tensor," *Flow, Turbulence and Combustion*, vol. 62, pp. 183–200, 1999.

[28] P. G. Tucker, *Numerical Methods*, p. 148–259. Cambridge Aerospace Series, Cambridge University Press, 2016.

[29] V. S. Balaji, A. De, and S. De, "Journal of energy and environmental sustainability numerical investigation of swirling hydrogen flames: Effect of swirl and fuel jet in coherent structures," 2016.

[30] I. B. Celik, Z. N. Cehreli, and I. Yavuz, "Index of resolution quality for large eddy simulations," vol. 127, pp. 949–958, 9 2005.

VITA

Kourosh completed his secondary education at Noordanesh in 2011. He then attended Islamic Azad University, receiving his bachelor's degree in mechanical engineering in 2016.

During his undergraduate studies, Kourosh developed a strong interest in various fields of Mechanical engineering. He participated in various research projects and completed a thesis titled "Modeling and Simulation of the 4-DOF Serial SCARA Robot" in 2016.

After five years of working experience and completing his military service, In 2021, Kourosh joined Mechanical Engineering at Özyeğin University, where he pursued his Master's degree in fluid mechanics. He researched TPMS structures, focusing on flow and heat transfer characteristics. His dissertation, titled "Numerical Analysis of Flow and Heat Transfer Characteristics of Gyroid Type Structures With Triply Periodic Minimal Surfaces," explores the flow and heat transfer characteristics within the Gyroid-type TPMS structures with various geometry frequencies.

Kourosh presented his research at the 9th International Symposium on Advances in Computational Heat Transfer conference.

In addition to his research, Kourosh has been a research assistant in the Department of Mechanical Engineering at Özyeğin University.

Kourosh Naji

09/08/2024